IOP Publishing Plasma Sources Science and Technology
Plasma Sources Sci. Technol. **27** (2018) 105020 (26pp) https://doi.org/10.1088/1361-6595/aadf5b

Electrode configurations in atmospheric pressure plasma jets: production of reactive species

Amanda M Lietz[1] and **Mark J Kushner**[2,3]

[1] University of Michigan, Department of Nuclear Engineering and Radiological Sciences, 2355 Bonisteel Blvd., Ann Arbor, MI 48109-2104 United States of America
[2] University of Michigan, Department of Electrical Engineering and Computer Science, 1301 Beal Ave., Ann Arbor, MI 48109-2122 United States of America

E-mail: lietz@umich.edu and mjkush@umich.edu

Received 23 June 2018, revised 22 August 2018
Accepted for publication 6 September 2018
Published 30 October 2018

Abstract

Atmospheric pressure plasma jets (APPJs) are a preferred plasma source for many biomedical applications. These jets typically consist of a rare gas flowing through a dielectric tube, possibly with an O_2 or H_2O admixture, and flowing into the ambient. They are typically powered by pulsed or sinusoidal voltage waveforms. However, in most other aspects APPJ designs differ greatly. In this paper, APPJ design parameters and their consequences on ionization wave (IW) propagation and reactive oxygen and nitrogen species (RONS) production are discussed using results from a two-dimensional plasma hydrodynamics model. The base case is an APPJ with a single powered ring electrode wrapped around a dielectric tube. This configuration was varied by adding a grounded ring electrode, changing the powered and grounded electrode positions, and moving the powered electrode to the inside of the tube. Placing the powered electrode closer to the outlet of the tube increased the RONS production by increasing the energy deposition outside the tube. Adding a grounded ring increased the IW intensity inside the tube while slightly increasing the power deposition outside of the tube. An inner powered electrode increased the IW intensity and propagation velocity, and the resulting RONS production. Co-axial ground planes within 5 cm of the APPJ significantly affected the IW behavior, increasing its intensity and increasing RONS production. The consequences of voltage rise time and dielectric constant of the tube are also discussed. The systematic trends from this investigation may facilitate more informed APPJ design choices that may be tailored to the goals of a specific application.

Keywords: atmospheric pressure plasma jet, modeling, plasma chemistry

1. Introduction

The reactive species produced by atmospheric pressure plasmas have been the focus of a recent body of work investigating their use for biomedical applications including wound healing, cancer treatment, and stimulating anti-tumor immune responses [1–6]. The effects of atmospheric pressure plasma jets (APPJs) on biological systems are often attributed to the reactive oxygen and nitrogen species (RONS) generated by the plasma, although electric fields and UV photons may also have significant influences [7, 8]. Differences in the precise assortment of RONS generated by different APPJs can affect the biological outcome. Although the ideal balance of RONS has not yet been determined and likely varies by biological system, there is evidence that OH, H_2O_2, $O_2(^1\Delta_g)$, and ONOOH all have important roles in cancer treatment [9–11]. APPJs have been preferred in many of these studies because their operation with rare gases keeps the gas temperatures low and enables greater control of the species that are generated compared to discharges in ambient air.

There is a large variety of APPJ designs, including electrode configurations that have pin and ring electrodes either

---

[3] Author to whom any correspondence should be addressed

inside or outside of the dielectric tube forming the jet, or some combination of electrodes located inside and outside [12]. In each design variation, an ionization wave (IW) propagates through and out of the tube and into the ambient air. A rare gas is usually flowed through the tube, either pure or with a small ($<2\%$) admixture of a molecular gas such as oxygen or water vapor [4, 13–15]. As the IW propagates out of the jet, the IW interacts with the ambient air, producing RONS. The gas flow carries the RONS to the surface or tissue being treated by the plasma. (Note, that even the purest rare gases available from gas suppliers have sufficient impurities to produce RONS inside the tube before the IW encounters the ambient.)

The large variety of designs and configurations makes optimizing APPJs for a particular application difficult, as is assessing the differences between observed biological effects achieved with different APPJ designs. Several experimental studies have examined the influence of APPJ design parameters on performance. Time resolved optical emission and electrical properties of APPJs were shown to be sensitive to electrode configuration by Maletic *et al* [16]. Increasing the contact area of ring electrodes around the dielectric tube of an APPJ increases the power coupled into the plasma at a given voltage. Jogi *et al* investigated the effect of tube diameter on a sub-mm jet with a single ring electrode. Increasing tube diameter did not require as high a voltage to sustain the discharge, increased the excitation temperature as measured by optical emission, and decreased the electron density [17]. Maletic *et al* also showed that for an APPJ with two outer ring electrodes, the distance the electrodes were placed from the end of the tube greatly affected the propagation distance of the IW into the ambient [18]. Yue *et al* have shown through laser induced fluorescence (LIF) measurements of an APPJ sustained in He that adding additional ring electrodes can increase the OH production by as much as a factor of 5, which in turn increases the bactericidal effects of the jet [19]. In two APPJs examined by Xu *et al*, the electrode configuration had a significant effect on the RONS produced in a liquid downstream of the jet [13].

Modeling studies of APPJs often focus on operational parameters rather than design parameters. Norberg, *et al* studied the effect of pulse repetition frequency (PRF), gas flow rate, and gas composition of an APPJ having a fixed geometry [20]. Van Gaens *et al* examined the consequences of gas flow rate, power, and ambient humidity using a 1D plug flow model [21]. Kelly *et al* investigated the outcome of changing the concentration of the O_2 in a He APPJ and the influence of the distance between the jet and the surface being treated for a fixed geometry of the APPJ [22].

The focus of this paper is on the consequences of physical and electrical design parameters, and of electrode configurations in particular, on the behavior of APPJs, including IW propagation and RONS production. Electrical ground surfaces that are integral components of the jet as well as distant (often unintentional) ground planes were investigated. Placing a coaxial ground within 5–6 cm of the jet increases the IW propagation speed and the production of all RONS for a constant voltage. Moving the powered ring electrode closer to the end of the tube also produces more RONS, as most of the RONS are produced outside of the tube. Adding a grounded ring electrode on the tube increases the initial IW speed and intensity, however both are significantly attenuated upon passing the grounded ring. Placing the powered electrode inside of the tube increases the IW speed. Generally, changes in electrode configuration which increase the total energy deposition (such as adding a grounded ring) also decrease the energy efficiency of the RONS production.

The model is described in section 2, while the results of our investigation are discussed in section 3. The base case is an APPJ with a single powered ring electrode outside of the tube powered by a negative voltage pulse. The other designs are variations of the base case. The discussion includes consequences of the radius of a coaxial ground, the position of the powered electrode along the tube, the addition of a grounded ring electrode (and distance between ring electrodes) and using a powered electrode inside the tube. The discussion concludes with examining the effects of electrical parameters including voltage rise time and the dielectric constant of the tube. Concluding remarks are in section 4.

2. Description of the model

The model used in this study, *nonPDPSIM*, is a two-dimensional plasma hydrodynamics model which is described in detail in [20]. The model uses time slicing algorithms to address the multiple timescales of the discharge and flow dynamics. The model includes a solution of Boltzmann's equation for the electron energy distribution (EED) to provide transport coefficients as a function of average electron energy, a solution of the compressible Navier–Stokes equations for fluid flow, and a radiation transport module. Poisson's equation is solved for the electrical potential, including applied voltages, charged species in the gas phase, surface charging, and different electrical solid material properties as expressed through dielectric constant and conductivity. The model utilizes an unstructured numerical mesh to enable greater spatial refinement in regions where the IW propagates and gradients in densities and electrical properties are large. The charged species densities and potentials are solved using a fully implicit algorithm with timesteps that are dynamically chosen, usually 1–10 ps during the active plasma portion of the simulation. The electron energy transport and conservation equation that provides the average electron energy is also implicitly solved following the update of densities and potential.

Boltzmann's equation is solved for the EED to provide electron impact rate and transport coefficients. The computational domain is divided into zones having different gas composition. In this case, one zone has the majority gas being helium, while the second zone has the majority gas being air. Boltzmann's equation for the EED is solved using a two-term spherical harmonic expansion in the electron density weighted gas composition of each zone. The two-term approximation is expected to provide accurate ionization rate coefficients within 10% at the highest E/N (electric field/gas number density) for our conditions [23]. This process provides the electron impact rate coefficients and electron temperature (T_e) as a function of the reduced electric field,

E/N. A lookup table is saved so that the electron impact rate coefficients can be interpolated as a function of T_e. Although the gas composition of each zone is nearly constant in time (the dissociation fraction is low), as the IW propagates out of the tube, the electron density weighted composition changes. This evolution necessitates an update to the lookup table, which was recalculated every 0.05 ns during the plasma calculation. In parametric studies of the required frequency for updating the lookup table, nearly identical results were obtained with 1 ns between updates.

The fluid module solves a modified version of the Navier–Stokes equations which uses gas density (and not mass density) in the continuity equation, and uses a mole fraction weighted mass density in the momentum equation to address the flow composition which is varying in space and time due to reactions and mixing between the He and air. The Navier–Stokes equations are solved implicitly using an unsteady algorithm. The fluid module approximates the system as having a single advective velocity which is used when updating the neutral and charged species densities. The total number density at each node is renormalized to the number density calculated by the fluid module after each call to the fluid. The neutral flow is allowed to reach a steady state before the plasma calculations begin, which takes 12 ms in these cases.

The radiation transport module uses a Green's function operator, where the maximum range of the photon is limited to 750 μm in order to reduce the computational cost. The photo-ionization processes included in these simulations are emission from the He excimer (He_2^*) ionizing N_2, O_2 and H_2O. The He_2^* is a lumped state of several excimers, and the photo-ionization cross sections for excimer radiation at 18 eV are used for N_2 (2.5×10^{-17} cm^2), O_2 (1.5×10^{-17} cm^2), and H_2O (2.3×10^{-17} cm^2) [24]. The integral of the Green's function is calculated once at the beginning of the calculation and not updated to reduce the computational burden. This is a reasonable approximation because the gas flow is stationary on the timescales of the plasma discharge. The photons emitted by excited states of the He monomer are highly trapped at these pressures due to reabsorption by abundant ground state He. The excimer emission does not experience resonant reabsorption, and can therefore produce non-local ionization. The contribution of photoionization of O_2 by emission from N_2^{**}, (the lumped state including $N_2(C^3\Pi_u)$ and $N_2(E^3\Sigma_g^+)$) was included in isolated cases and determined to be inconsequential for the conditions of this study.

Since the description of the model found in [20], several updates to the algorithms for implicit charged particle transport have been made to improve the performance and stability of the model. The solutions of Poisson's equation, the densities of charged species and charge densities on and in non-plasma materials are simultaneously performed using an implicit Newton's iterations technique, as described in [21]. The numerically most time-consuming portion of the simulation requiring the shortest timestep is solving for the charged species densities and electric potential at each node.

To obtain implicitness in the solution for charged species densities and potentials, Jacobian elements are included in the resulting matrix. These Jacobian elements are, for example, $\partial n_{ki}/\partial n_{mj}$, the incremental change in the density of a species k at node i due to a change in density of species m at neighboring node j. In the previous formulation, a perturbation technique was used to compute the values of Jacobian elements. In this technique, for timestep Δt

$$\frac{\partial n_i}{\partial n_j} = \Delta t \frac{\lfloor dn_i(n_j)/dt - dn_i(n_j + \Delta n_j)/dt \rfloor}{\Delta n_j}, \tag{1}$$

where Δn_j is a small perturbation in the value of n_j. (To simplify notation, we consider Jacobian elements of a single species with its own density at a neighboring node.)

The resulting system of equations is iteratively solved using different sparse matrix operators depending on the properties of the resulting matrix. The system we solve is

$$\overleftrightarrow{F}\vec{x} = \vec{b}, \tag{2}$$

where $\overrightarrow{x}$ is an array of the potentials, charged species densities and surface charge densities at every node in the mesh. $\overleftrightarrow{F}$ is a matrix containing the finite-volume form of the partial derivatives representing the transport equations including the Jacobian elements. Since a Newton-iterations method is being used to refine the solution, $\vec{b}$ is the residual of the potential or charged species density, which reduces to 0 as the solution converges. This problem is solved iteratively, until the residual is below the maximum allowed error, generally requiring 5–10 iterations for each timestep. The system of equations minimizes a residual, rather than directly solving for the species densities and potentials. The elements of $\overleftrightarrow{F}$ can be described in terms of the physical Jacobian elements in equation (1) by

$$F_{ij} = \frac{1}{\Delta t}\left(\delta_{ij} - \frac{\partial n_i}{\partial n_j}\right), \tag{3}$$

where n_i and n_j are a density of a charged species or a potential at any neighboring node and $\delta_{ij} = 1$ if $i = j$ and 0 otherwise. For clarity, the discussion that follows will be in terms of the more physically intuitive partial derivatives rather than the matrix elements. These include the partial derivative of potentials with respect to charged species densities ($\partial\Phi_i/\partial n_i$, $\partial\Phi_i/\partial n_j$), as well as the derivatives of densities with respect to densities at other nodes and the potentials ($\partial n_i/\partial n_j$, $\partial n_i/\partial\Phi_i$, $\partial n_i/\partial\Phi_j$). The Jacobian elements between node-pairs for potentials depend only on geometry and permittivity of materials. Those Jacobian elements can be computed once and stored. The matrix elements containing partial derivatives of densities or surface charges change with each Newton-iteration and their calculation should be as efficient as possible. In this regard, the previous numerical method to compute Jacobian elements was replaced with closed form expressions.

The equation being solved by this matrix formulation, is the density of charged species s at node i given by

$$n_{si}(t_1) = n_{si}(t_0) + \Delta t\left(S_{1si}n_e(t_1) + S_{2si} + \sum_j \Gamma_{sij}(t_1)\frac{A_{ij}}{V_i}\right), \tag{4}$$

where t_0 refers to the previous time at which the solution was obtained, t_1 is the time at which the solution is desired and $\Delta t = t_1 - t_0$. $n_{si}(t_1)$ is the working density at the current time that becomes increasingly accurate with each Newton iteration. $\Gamma_{sij}(t_1)$ is the flux of species s from node i to neighbor j based on the current solution, A_{ij} is the area of interface between a cell and its neighbor j, and V_i is the volume associated with the current node. S_{1si} is the source of species s at node i due to electron impact processes, which is updated at every iteration. S_{2si} is the source of species s at node i that is independent of electron density, for example due to photo-ionization or Penning ionization. In order to tune the implicitness of the scheme to the particular problem, the parameter β is used, where $\beta = 0$ is fully explicit and $\beta = 1$ is fully implicit. The more general equation becomes

$$n_{si}(t_1) = n_{si}(t_0) + \Delta t\Bigg([\beta n_e(t_1) + (1-\beta)n_e(t_0)]S_{1si} + S_{2si} + \sum_j(\beta\Gamma_{sij}(t_1) + (1-\beta)\Gamma_{sij}(t_0))\frac{A_{ij}}{V_i}\Bigg). \quad (5)$$

The fluxes for charged particles are provided by a modified version of the formulation developed by Scharfetter and Gummel [25]

$$\Gamma_{sij} = \alpha\left(\frac{D_{si}+D_{sj}}{2}\right)\frac{n_{si} - n_{sj}\exp(\alpha\Delta x_{ij})}{1-\exp(\alpha\Delta x_{ij})}, \quad (6)$$

$$\begin{aligned}\alpha &= \frac{-q(\mu_{si}+\mu_{sj})(\Phi_i - \Phi_j) - 2v_{ij}}{(D_{si}+D_{sj})\Delta x_{ij}} \\ &= \frac{-q(\mu_{si}+\mu_{sj})E_{ij} - 2v_{ij}}{(D_{si}+D_{sj})},\end{aligned} \quad (7)$$

where D_{si} is the diffusion coefficient of species s at node i, and μ_{si} is the mobility of species s at node i. Φ_i is the electric potential at node i. v_{ij} is the fluid velocity assuming that ions are entrained in the bulk fluid flow, and E_{ij} is the electric field along the chord from node j to node i. Δx_{ij} is the chord length between the node and its neighbor.

The real values of the species densities, potentials, charge densities, and matrix elements could vary by many orders of magnitude, which makes for difficulty in the linear algebra. In order for these values to be closer to the same order of magnitude, all densities and potentials are globally normalized by an expected value.

The previous perturbative technique used a function which returns a normalized value of the residual b to compute the normalized matrix element, F_{ij}. If the perturbation is too small, the change in b may be below precision limits. If the perturbation is too large, the derivative will not be accurate. The perturbative calculation results in unnecessary effort. For example, only one term in the summation of fluxes over faces in equation (5) will contribute to the matrix element for any pair of mesh points.

As an improvement to the perturbation technique, analytical derivatives are calculated directly for potentials and densities. These analytical derivatives are shown below where all time dependent variables refer to the value at t_1. The Jacobian element for density at the central node is

$$\frac{\partial n_{si}}{\partial n_{si}} = \beta\sum_j\left[\frac{\alpha(D_{si}+D_{sj})}{1-\exp(\alpha\Delta x_{ij})}\right]\frac{A_{ij}}{V_i}\Delta t. \quad (8)$$

This calculation becomes less accurate at small values of α, where the denominator goes to zero. If $\alpha\Delta x_{ij} < 10^{-4}$, the analytical limit is used

$$\lim_{x\to 0}\frac{x}{1-e^x} = -1, \quad (9)$$

$$\frac{\partial n_{si}}{\partial n_{si}} = \sum_j^{\text{neighbors}}\frac{\beta A_{ij}\Delta t(D_{si}+D_{sj})}{2V_i} \times\begin{cases}\dfrac{\alpha}{1-\exp(\alpha\Delta x_{ij})} & \alpha\Delta x_{ij} \geq 10^{-4} \\ -\dfrac{1}{\Delta x_{ij}} & \alpha\Delta x_{ij} < 10^{-4}\end{cases}. \quad (10)$$

A small α indicates a small electric field for which transport converges to diffusion as α approaches zero. The application of the limit produces errors that are less than 0.01%. The maximum allowed value of $\alpha\Delta x_{ij}$ is 500, a value for which the magnitude of the denominator is sufficiently large to properly represent the transport. A similar limit is applied to the derivative with respect to the density at the neighboring node.

$$\frac{\partial n_{si}}{\partial n_{sj}} = -\frac{\Delta t\beta A_{ij}(D_{si}+D_{sj})}{2V_i} \times\begin{cases}\dfrac{\alpha\exp(\alpha\Delta x_{ij})}{1-\exp(\alpha\Delta x_{ij})} & \alpha\Delta x_{ij} \geq 10^{-4} \\ -\dfrac{1}{\Delta x_{ij}} & \alpha\Delta x_{ij} < 10^{-4}\end{cases}. \quad (11)$$

Due to the second term in equation (4), which represents electron impact reactions, the derivative with respect to the electron density must also be included in the matrix

$$\frac{\partial n_{si}}{\partial n_e(t_1)} = -\Delta t\beta S_{1si}. \quad (12)$$

In the case of electrons, this is added to the matrix element in equation (10), but for all other species, this is an additional matrix element.

The derivatives with respect to potentials are slightly more complicated because α is a function of potential

$$\frac{\partial n_{si}}{\partial \Phi_i} = -\sum_j\frac{\Delta t\beta A_{ij}}{V_i}\frac{q(\mu_{si}+\mu_{sj})}{2\Delta x_{ij}} \times\begin{cases}\dfrac{n_{si}-n_{sj}\exp(\alpha\Delta x_{ij})}{1-\exp(\alpha\Delta x_{ij})} + \dfrac{(n_{si}-n_{sj})\alpha\Delta x_{ij}\exp(\alpha\Delta x_{ij})}{(1-\exp(\alpha\Delta x_{ij}))^2} & \alpha\Delta x_{ij} \geq 10^{-3} \\ \dfrac{n_{si}+n_{sj}}{2} & \alpha\Delta x_{ij} < 10^{-3}\end{cases}. \quad (13)$$

The derivative of the density with respect to the potential at a neighboring node is simply the negative of the function above, without summing over the neighbors

$$\frac{\partial n_{si}}{\partial \Phi_j} = \frac{\Delta t \beta A_{ij}}{V_i}\frac{q(\mu_{si}+\mu_{sj})}{2\Delta x_{ij}} \times \begin{cases} \dfrac{n_{si}-n_{sj}\exp(\alpha\Delta x_{ij})}{1-\exp(\alpha\Delta x_{ij})} + \dfrac{(n_{si}-n_{sj})\alpha\Delta x_{ij}\exp(\alpha\Delta x_{ij})}{(1-\exp(\alpha\Delta x_{ij}))^2} & \alpha\Delta x_{ij} \geq 10^{-3} \\ \dfrac{n_{si}+n_{sj}}{2} & \alpha\Delta x_{ij} < 10^{-3} \end{cases}. \quad (14)$$

Applying the analytical limit at $\alpha\Delta x_{ij} = 10^{-3}$ results in errors $<0.1\%$ compared to the exact solution.

When implementing these expressions, the more accurate analytic Jacobian elements resulted in computational speed-ups as much as a factor of 4. With more accurate Jacobian matrix elements, the solution converged in fewer iterations, leading to the ability to take larger timesteps without increasing the error or decreasing the stability.

3. Consequences of APPJ design parameters on RONS production

3.1. Base case

The base case geometry, shown in figure 1(a), is a quartz tube with an external powered ring electrode wrapped around the exterior 8 mm from the end of the tube and covered by a thin layer of dielectric. The geometry is cylindrically symmetric containing 12,572 nodes with 9,268 nodes in the plasma region. The tube and material covering the electrode have a relative dielectric constant of $\varepsilon_r = 4$ (where dielectric constant $\varepsilon = \varepsilon_r\varepsilon_0$, and ε_0 is the permittivity of free space). The top surface of the computational domain, 1.55 cm from the end of the tube, is electrically grounded and acts as a pump. This surface should be thought of as a fine metal mesh with spacing not resolved in the model. The radial boundary of the domain is also an electrical ground which is 1.44 cm in radius in the base case, and is referred to as the coaxial ground. In studies discussed below, the diameter of the coaxial ground was varied. In order to minimize the possibility that small changes in the numerical mesh could affect the computed results as the diameter of the coaxial ground was changed, the following procedure used. A numerical mesh was created for the largest diameter of the coaxial ground, as shown in figure 1(b). Annular zones were also defined in the mesh having diameters corresponding to the coaxial grounds to be studied. These zones could be defined as being either metal or dielectric (i.e., air) while not changing the underlying numerical mesh. A second grounded ring electrode was also used in the study, shown in figure 1(b). Its electrical properties were controlled by specifying its material properties to be metal for an active electrode or dielectric with $\varepsilon_r = 1$ without changing the mesh or modifying the gas flow. Several refinement zones were included in the mesh to better resolve the regions where the plasma would be propagating, resulting in a mesh spacing of approximately 50 μm inside the tube, as shown in figure 1(c).

He with impurities of $O_2/H_2O/N_2 = 2.4/2.9/4.7$ ppm was flowed through the tube from an inlet on the bottom boundary of the computational domain. These impurities were chosen based on the specifications provided by a gas supplier for He having 99.999% purity. Humid air with $N_2/O_2/H_2O = 79.5/20/0.5$ (14% relative humidity) flowed from the annular face on the bottom boundary of the computational domain coaxial to the tube. The He flowed at 2 slm and the air at 4 slm. The pressure was maintained at 1 atm at the face of the pump. The steady state gas flow was established by running only the fluid module of the model for 12 ms before pulsing the negative voltage on the powered electrode to initiate the plasma. The He density of this steady state flow is shown in figure 2(a). The flow velocity on-axis at the end of the tube is 1.1×10^4 cm s^{-1}, and the Reynolds number is ≈350, which is well within the laminar flow regime. As the He flows out of the jet, humid air diffuses into the helium plume, also shown in figure 2(a).

The reaction mechanism is documented in [26], and contains 51 species addressing helium and humid air, and 753 reactions. In the following discussion, N_2^* is a lumped state including $N_2(A^3\Sigma)$, $N_2(B^3\Pi)$, $N_2(W^3\Delta)$, $N_2(C^3\Sigma)$, $N_2(a'^1\Sigma)$, $N_2(a'^1\Pi)$, $N_2(w^1\Delta)$. N^* represents $N(2^2D)$ and $N(2^2P)$, O_2^* represents $O_2(^1\Delta)$ and O_2^{**} represents $O_2(^1\Sigma)$. Excitation into the first 8 vibrational levels is lumped into the state $N_2(v)$.

As shown in global modeling by Schröter *et al*, surface reaction probabilities are generally not well characterized and can influence the long-term chemistry [27]. In this work, all ions are assumed to neutralize at surfaces, leaving charge on the surface. Excited states were assumed to be quenched at surfaces with unity probability, except $N_2(v)$, O_2^*, and O_2^{**} which have quenching probabilities of 0.5, 10^{-5}, and 0.1. Neutral recombination probabilities on surfaces are assumed to be 0.01 for $N \rightarrow ½N_2$, 0.02 for $O \rightarrow ½O_2$, 0.2 for $H \rightarrow ½H_2$, and 0.2 for $OH \rightarrow ½H_2O_2$. All other ground state neutral species do not undergo surface reactions.

The full plasma dynamics including solution of Poisson's equation were simulated for 200 ns, which includes a negative pulsed voltage applied to the powered electrode and a short afterglow. After this period, the plasma is assumed to be neutral at all spatial points, while continuing to react and

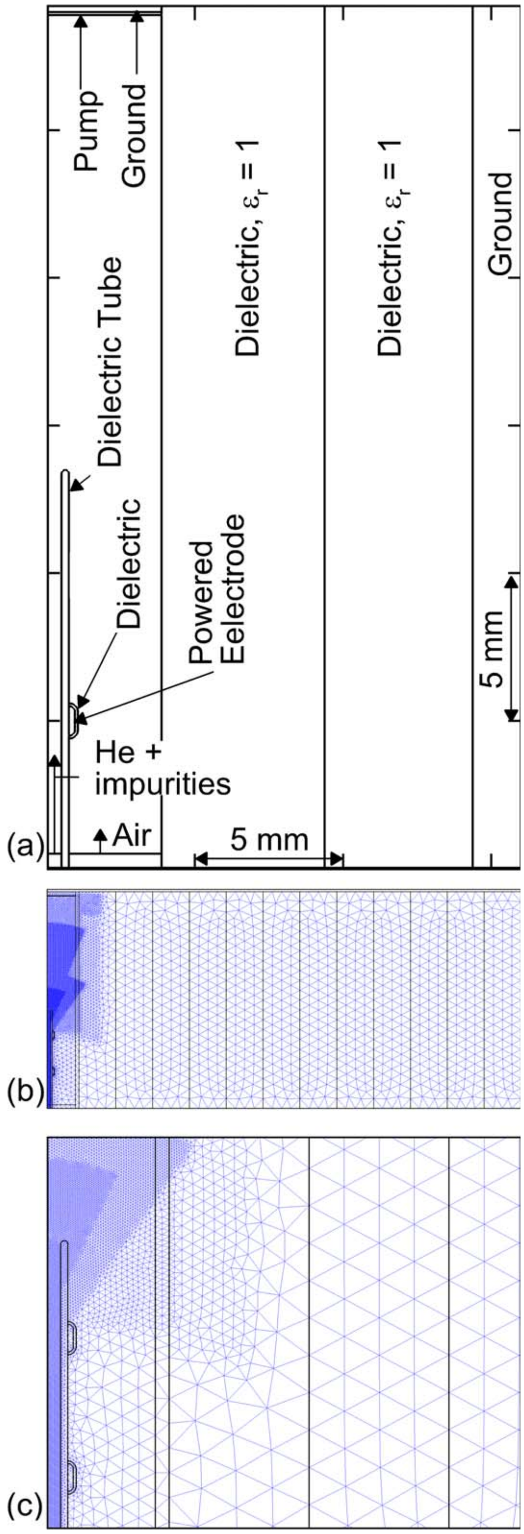

Figure 1. Schematic of the setup for the base case. (a) The geometry, with a dielectric tube inner diameter of 1 mm. The powered electrode is an external ring. (b) The geometry extends beyond the figure in the radial direction, and the thickness of the radial dielectric can be varied so that the distance to the radial ground plane is also varied. The powered electrode is covered with a thin dielectric with $\varepsilon_r = 4$. (c) The computational mesh with refinement zones inside the tube and in regions of higher helium concentration.

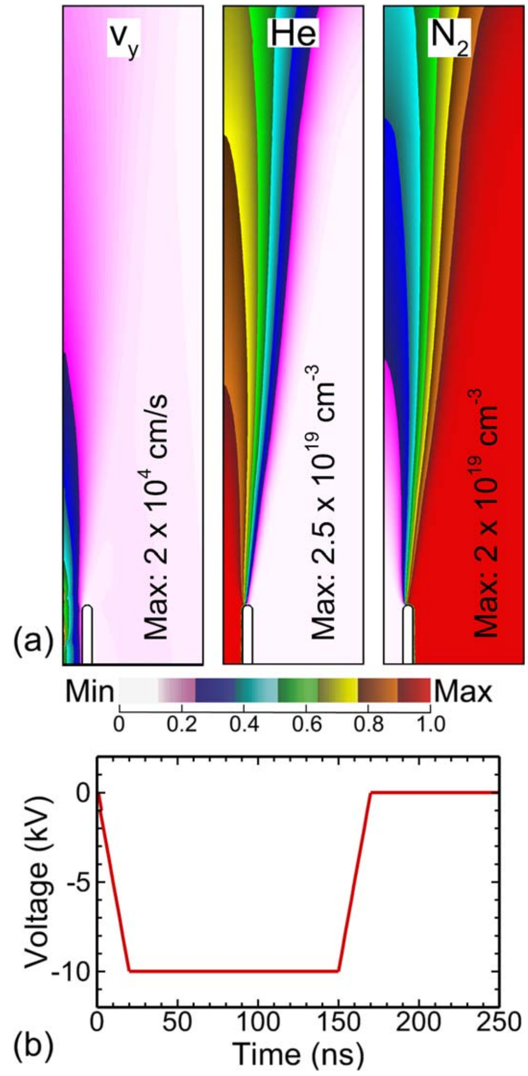

Figure 2. Fluid and electrical properties for the simulation. (a) The steady state gas flow profile after 12 ms: (left) axial velocity, (center) He density, and (right) N_2 density. The scales are linear, and the maximum value is listed in each frame. As the He flows into the ambient, humid air begins diffusing in to the helium, the velocity profile broadens due to the viscosity of the fluid causing entrainment. (b) The negative voltage pulse waveform applied to the powered electrode.

recombine. Poisson's equation is then no longer solved and the charged species diffuse with an effective ambipolar diffusion coefficient. During this period, the electron temperature is fixed at 0.025 eV. This procedure significantly decreases the computational expense while allowing the charged species to persist and continue to influence the chemistry. The calculation is continued in this mode for 4 ms at which time all reactive species have flowed out of the computational domain. A single discharge pulse and afterglow were computed. As species pass through the plane of the pump, their fluxes are integrated over the area of the face of the pump and in time. This integration provides a total fluence of reactive species produced by a single discharge pulse that would conceptually be available for treating a surface located at approximately the height of the pump plane.

With the flow rates and residence times investigated in these simulations, the details of the results strictly apply to an APPJ having a PRF no higher than 250 Hz. At these PRF, all plasma produced species will have flowed out of the computational domain prior to the next pulse. As discussed by Norberg, *et al* [20], operating at higher PRFs introduces the possibility that RONS produced during a current discharge pulse react with the species produced during previous pulses that have not yet flowed out of the domain. These conditions favor production of more complex (H)NO$_x$ over simpler species such as NO. At the same time, the properties of the IW that are sensitive to geometry (as discussed here) and material properties are weak functions of PRF. The results of this investigation therefore broadly apply to higher PRF.

The pulsed voltage applied to the powered electrode, shown in figure 2(b), has a total duration of 170 ns and a maximum amplitude of -10 kV. The voltage has a 20 ns rise time, followed by 130 ns at the maximum amplitude and terminates with a 20 ns fall time. The full plasma calculation continues 30 ns after the voltage returns to zero, for a total of 200 ns. At the beginning of the plasma calculation, a small cloud of plasma with a peak electron density of 1×10^{11} cm^{-3} is placed inside the tube near the powered electrode. This initial density of the electron cloud has an exponential spatial distribution with a characteristic length of 100 μm in the radial direction, and 300 μm in the axial direction. The plasma is neutralized by a density of He$^+$ and O$_2^+$ equal to that of the electrons.

The preionization electron density of 10^{11} cm^{-3} applies to only a small region near the powered electrode to initialize the discharge, and contains approximately 10^7 electrons. This number of electrons is large enough to initiate the discharge but small enough that it does not affect the end result. Changing the density for the initial seed did not affect the behavior of the IW or the resulting chemistry. At worst there are minor differences during the first few ns of the discharge, which dissipate once the IW develops. The precise choice of ions to balance the electrons, in this case He$^+$ and O$_2^+$ also has no significant impact on the results. After the discharge develops, the positive ion density in the preionization region is as high as 10^{14} cm^{-3}, compared to the 10^{11} cm^{-3} that was used to initiate the discharge.

This study was not intended to replicate the results of any single experiment. Rather the study was intended to systematically investigate the consequences of varying experimentally accessible parameters, such as electrode placement, materials and voltage waveforms, in a manner that has not yet been experimentally performed. As such, data are not available to make side-by-side comparisons to experiments—such studies have not been comprehensively performed using similar enough devices to enable such comparisons. That said,

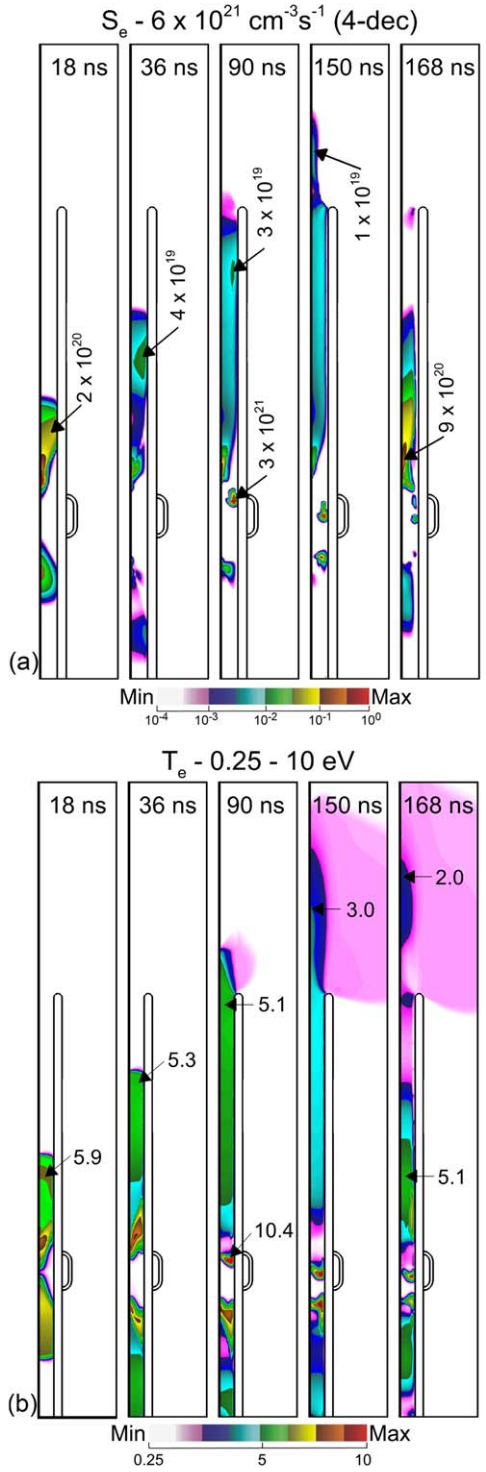

Figure 3. Ionization wave (IW) propagation in the base case. (a) The electron impact ionization source term (S_e) shows the IW propagating in both directions, though primarily towards the outlet of the tube. At 150 ns as the applied voltage begins to fall, a restrike occurs producing a second IW inside the tube. (b) Electron temperature and as the ionization wave propagates. After 90 ns, the plasma begins interacting with the ambient air, T_e decreases and the IW propagation slows. At 168 ns, as the voltage decreases, T_e increases. S_e is shown on a four-decade log scale. T_e is shown on a linear scale.

throughout the following discussion, comparisons are made to experimental data for similar devices, acknowledging that in this diversity of data from different devices, geometries and operating conditions, there are no precise replicates to the systematic study performed here.

The plasma is produced by an IW which propagates through the tube and into the He dominated plume, as discussed in previous studies [28]. The IW is primarily driven by electron impact ionization, and the electron impact source term (S_e) is shown in figure 3(a). During propagation of the IW in the tube, the S_e at the leading edge of the IW has values of 2×10^{19}–3×10^{20} $\mathrm{cm^{-3}\,s^{-1}}$, sustained by an E/N of 30–50 Td (1 Td = 10^{-17} V $\mathrm{cm^2}$). In the plasma column created by and trailing the IW, $S_e \approx 1 \times 10^{19}\,\mathrm{cm^{-3}s^{-1}}$ and $E/N \approx 20$ Td. The IW propagates inside the tube with an annular shape, and the maximum electron impact ionization occurs near the surface of the dielectric tube. As the IW exits the tube, the maximum S_e follows the interface between the helium and the ambient air, converging on the axis 1.5 mm from the end of the tube. The lower threshold energies for inelastic collisions, including vibrational and electronic excitation of N_2, O_2, and H_2O, cause S_e in the IW front to decrease after exiting the tube. After 150 ns, the voltage begins to fall. This leads to a discharge which neutralizes the charge accumulated on the dielectric tube. At this point, there is a second burst in S_e as high as 9×10^{20} $\mathrm{cm^{-3}\,s^{-1}}$ in the conductive channel formed by the plasma, as current flows in the opposite direction—a restrike [29].

As shown in figure 3(b), the IW propagates with a steadily decreasing electron temperature (T_e), due to the charging of the dielectric tube near the powered electrode, which shields out some of the applied voltage. This is conceptually the behavior of a dielectric barrier discharge. T_e decreases more rapidly as the IW contacts the in-diffusing air due to electron energy losses to exciting low threshold energy vibrational and electronic states. There is an elevated T_e inside the tube, where a conductive channel enables current to flow through the plasma to neutralize the charged surface. T_e is substantially higher near the powered electrode (11.1 eV versus 5.8 eV) due to a positive IW driven by photoionization in this region. The electron density (n_e) increases during the period of the applied voltage, as well as immediately after the voltage drops when the plasma current is flowing in the opposite direction to neutralize the surface charge (the restrike), as shown in figure 4(a). The electron density continues to increase until 200 ns due to ionization processes which occur in the afterglow, such as Penning ionization. The electron density decreases by an order of magnitude by 10 μs after the voltage pulse due to both recombination and attachment.

The space charge density, appearing in figure 4(b), shows the initialization of the IW by charge separation. The IW contains a negative space charge due to the negative applied voltage, while positive charge accumulates in the vicinity of and on the surface of the tube at the powered electrode,

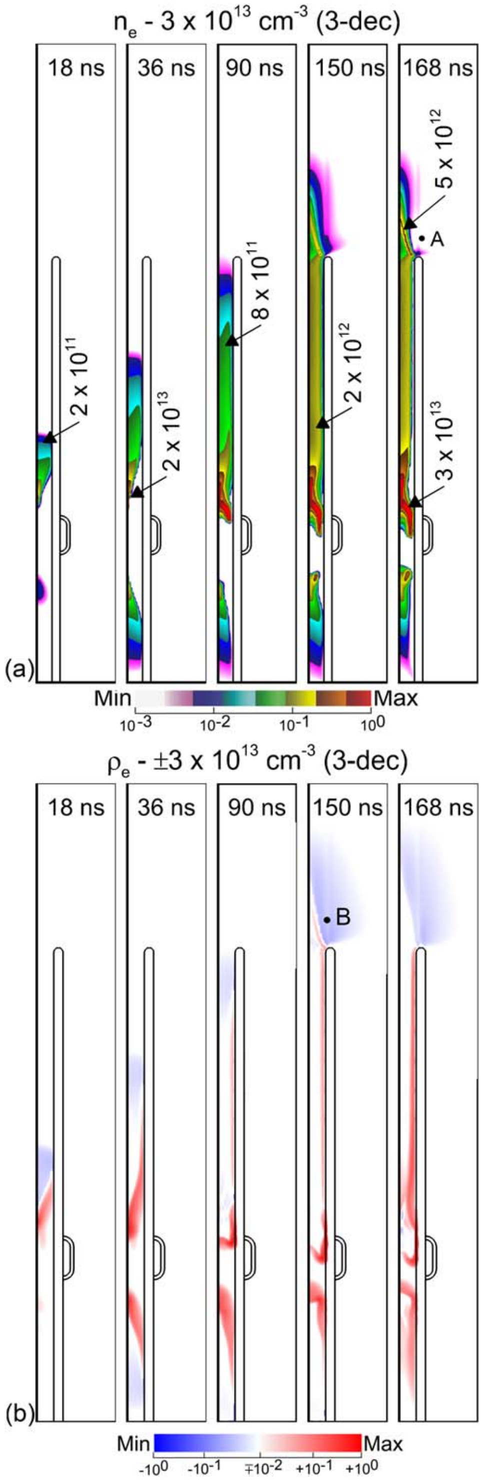

Figure 4. Charged species dynamics during IW propagation for the base case. (a) Electron density (n_e). Upon exiting the tube, the electron density transitions from annular to axial due to interactions with in-diffusing air. A high electron density develops close to the powered electrode. (b) Total space charge. The negatively charged streamer head negatively charges the inner wall of the tube as the IW propagates. A sheath forms inside the tube with the walls charged negatively and a layer of positive space charge in the gas. Quantities are shown on a three-decade log scale with maximum values indicated.

progressively screening out the applied voltage. In the rest of the tube, the surface negatively charges resulting in an electropositive plasma, and a sheath containing positive space charge forms in the plasma near the surface. Upon exiting the tube, the positive charge remains in the area of the highest plasma density, while the more mobile electrons diffuse out into the humid air.

As a result of the annular distribution of S_e inside the tube, the peak electron density is also annular, with the exception of the region in the vicinity of the powered electrode. Outside the tube during the voltage pulse, the electron density is more diffuse than the positive ions, a result of their higher temperature and mobility. This produces a net space charge where the electrons diffuse out of the ion containing region, with a charge density up to -2×10^{11} cm^{-3} and an electron density of approximately 3×10^{11} cm^{-3} (label B in figure 4(b)). This large space charge can be maintained because of the negative polarity of the applied electric field. When the magnitude of the applied voltage begins to decrease, the electrons in contact with humid air quickly attach to oxygen forming O_2^-, shown by the lack of electrons at label A in figure 4(a). In the regions of higher helium density, the electron density continues to increase even after the voltage is terminated (200 ns).

The structure in the plasma near the powered electrode is partly due to the photoionization model. He_2^* is initially produced near the powered electrode, and the resulting VUV radiation propagates isotropically, both upwards towards the end of the tube and downwards towards the gas inlet. Due to the impurities in the helium, photoionization occurs both above and below the powered electrode. This seed ionization then produces a cathode-directed IW, which propagates more slowly (downwards in the figures) than the primary anode directed IW (traveling upwards in the figures). The cathode directed IW occurs with an E/N of approximately 500 Td (5×10^{-15} V cm^2). The IW begins on axis, where the initial ionization seed was placed, propagates directly toward the powered electrode and upon reaching the surface of the dielectric tube, propagates along the surface as a surface ionization wave (SIW). This sequence generates a cathode-fall like structure at the inner surface of the tube at the powered electrode.

The ions and excited states produced by the plasma are shown in figure 5. The most abundant positive ions during the voltage pulse are He_2^+ inside the tube, and N_4^+ and O_2^+ outside the tube. He_2^+ is a result of electron impact ionization of He followed by dimerization, $He + He^+ + M \rightarrow He_2^+ + M$, where M refers to a third body which is dominantly He inside the tube. N_4^+ is a result of Penning ionization of N_2 by He^*, electron impact ionization, or to a lesser extent charge exchange from He^+ to N_2, followed by dimerization $N_2 + N_2^+ + M \rightarrow N_4^+ + M$. O_2^+ is primarily a result of Penning ionization by electronically excited helium. During the afterglow, the He_2^+ inside the tube charge exchanges to form O_2^+ in approximately 20 μs. After the voltage is turned off, the O_2^+ begins to dominate the N_4^+ outside of the tube and O_2^+ is the dominant positive ion for the remainder of the simulation. Although water cluster ions would be expected to form, they were not included in this reaction mechanism due to the computational cost of including a large number of ions [30, 31]. Given the small amount of water impurity inside the tube, water cluster ions would form in several microseconds, and therefore would not affect the IW or energy deposition dynamics. Outside the tube, where the water concentration is higher, cluster ions could form in tens of ns. The simplified reaction mechanism may lead to an underestimation of the recombination rates, but the neutral RONS produced in electron–ion recombination or ion–ion neutralization are generally independent of the additional water molecules present in higher order clusters [30].

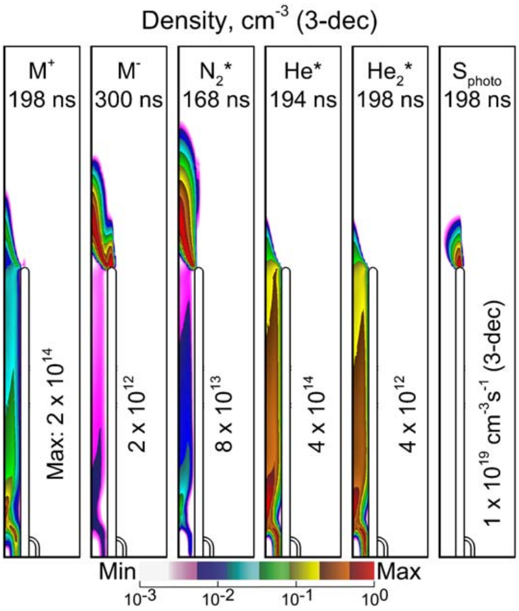

Figure 5. Total positive and negative ion density, shown at the time where they reach their maximum density. Several excited state species and the photoionization term are also shown. N_2^* is a lumped state including $N_2(A^3\Sigma)$, $N_2(B^3\Pi)$, $N_2(W^3\Delta)$, $N_2(C^3\Sigma)$, $N_2(a'^1\Sigma)$, $N_2(a'^1\Pi)$, $N_2(w^1\Delta)$. He^* is the sum of the electronically excited states $He(2^3S)$, $He(2^1S)$, $He(2^3P)$, $He(2^1P)$, and the lumped states He(3P) and He(3S). Photoionization is due to He_2^* ionizing humid air. Quantities are shown on a three-decade log scale with maximum values indicated.

Outside of the tube, O^- dominates in regions where the mole fraction of helium exceeds 87%, while O_2^- dominates in the regions containing more air. This change in dominant negative ion is due to the lower electron temperature in regions with higher mole fractions of air. Electron attachment forming O_2^- occurs with thermal electrons, while dissociative attachment to form O^- has a threshold energy of 4.3 eV. Within 100 ns of the end of the plasma period, most of the O^- has neutralized with positive ions. Any electron attachment that occurs by the thermal electrons during the afterglow forms O_2^-, which is therefore the dominant negative ion everywhere at this time. The plasma becomes an ion–ion plasma approximately 150 μs after the voltage pulse. The total ion densities are less than 10^8 cm^{-3} as the quasi-neutral cloud of ions exits the computational domain through the pump.

Although the ion–ion plume exiting the computational domain in this model is charge neutral, that assumption requires sufficient charge in the plume to produce the required ambipolar electric fields to maintain the charge neutrality. These ambipolar electric fields are typically associated with electron–ion plasmas and result from the differences in mobilities and temperatures of the negative (electrons) and positive (ions) charge carriers. When the total electron or ion density falls below a critical value, the maximum net charge in the plasma is insufficient to produce the ambipolar electric fields required to maintain charge neutrality (actually, quasi-neutrality). At that point, diffusion transitions to being free, and charge separation can occur. Ambipolar electric fields will also be produced in an ion–ion plasma if the mobilities or temperatures of the negative and positive ions are different, as will be the case in APPJs. As the total ion density decreases in the plume below the critical value to maintain charge-neutral fluxes, the negative and positive ions will separately freely diffuse. For simplicity, the model enforces charge neutrality in the afterglow, while in reality the dynamics would transition to free diffusion as neutralizing collisions deplete the ion density.

The densities of the more abundant excited states are shown in figure 5. The He excited states are most populous in areas containing less than 1% humid air. The helium excited states of He(2^3S), He(2^1S), He(2^3P) and He(2^1P) are explicitly included in the model, and all states above He(3^3S) and He(3^3P) are lumped into those two states. These states are dominantly formed by electron impact excitation of ground state He. In figure 5, He^* refers to the sum of all of these explicit and lumped states. He(2^3S) is the most abundant of these states both inside and outside of the tube, as it has the lowest energy and does not radiate. Each of the He excited states can combine with ground state He to form a dimer by the reaction $He^* + He + M \rightarrow He_2^* + M$. The state He_2^* is itself a lumped state including several excimers. The photons emitted by He_2^* are the most important with respect to photoionization. These VUV photons are not reabsorbed by ground state He, have a long mean free path and so can produce non-local photoionization. For this reason, radiation transport was included only for the excimer emission. Radiation trapping factors accounted for the emission of resonant radiation. The photoionization source, shown in figure 5, is defined by the extent of transport of the VUV photons and the influx of humid air that absorbs the radiation. Even at its peak ($2 \times 10^{19}\ \mathrm{cm^{-3}\ s^{-1}}$), the photoionization source is small compared to that due to electron impact ionization though photoionization may occur in regions where electron impact ionization is small. The photoionization source in the tube due to ionization of impurities is small in comparison ($8 \times 10^{14}\ \mathrm{cm^{-3}s^{-1}}$).

The densities of key reactive oxygen species (ROS) and reactive nitrogen species (RNS), shown in figure 6, reach their maxima at different times. The density of O is maximum at $2 \times 10^{13}\ \mathrm{cm^{-3}}$ at about 61 μs after the beginning of the plasma pulse. Most O is produced at the He/air interface

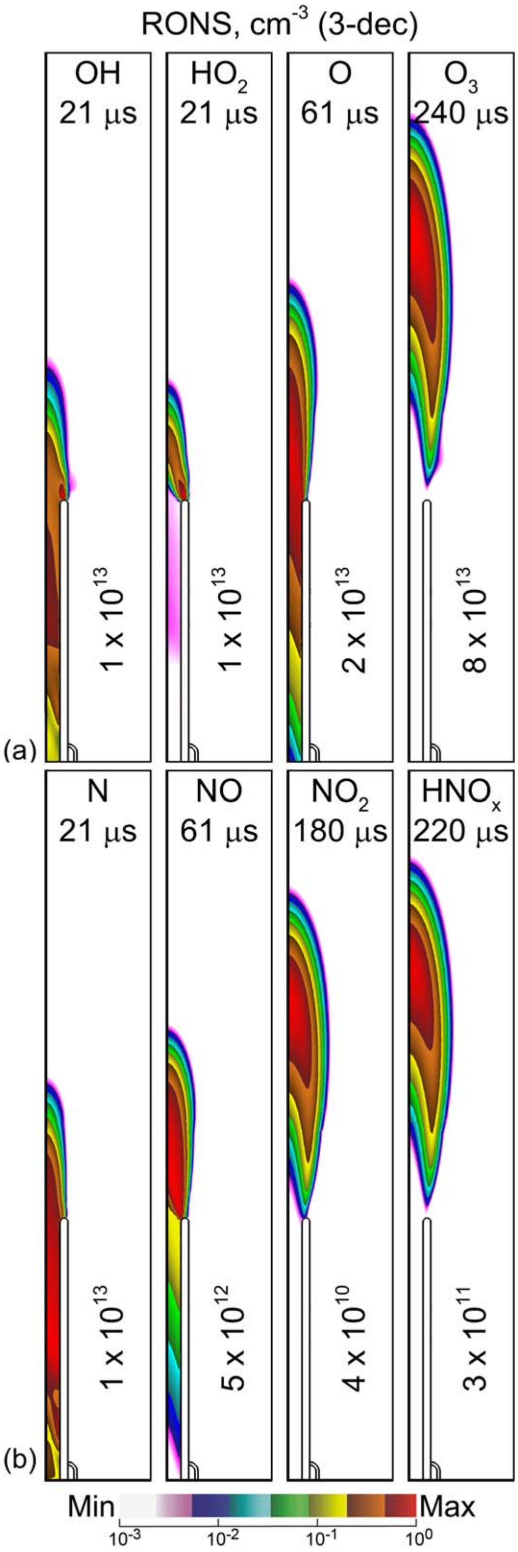

Figure 6. The most abundant species formed in the afterglow at the time of their maximum density. (a) Species which do not contain nitrogen (OH, HO_2, O, O_3) and (b) nitrogen containing species (N, NO, NO_2, HNO_x). This sequence of maxima in densities illustrates the conversion of initial reactive species to intermediate and terminal reactive species in time as the gas flow convects the species downstream. Species are shown on a three-decade log scale, with the maximum density and time at which that density occurs indicated on each frame.

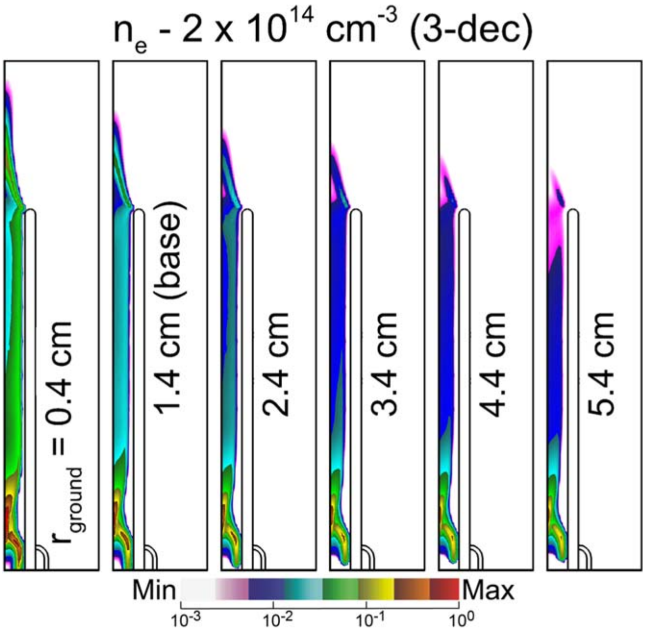

Figure 7. Electron density at 168 ns for jets with increasing radius of the coaxial ground plane. Having a nearby ground plane increases the IW velocity and results in more ionization outside of the tube, where many of the RONS are produced. n_e is shown on a three-decade log scale, and the radius of the coaxial ground is indicated on each frame.

outside the tube. During propagation of the IW, O is formed by electron impact dissociation, and dissociative attachment to O_2. Later in time, when the IW propagates through the He/air interface and produces excited states of nitrogen, $N_2^* + O_2 \rightarrow N_2 + O + O$ produces O, as does the ion–ion neutralization $O_2^- + O_2^+ \rightarrow O_2 + O + O$. O atoms are produced to a lesser extent in the tube by electron impact dissociation of impurity O_2. O_3 production results from three body reactions of O and O_2. There is a longer delay in the formation of O_3 for two reasons. First O_3 formation is a two-step process, and so it simply takes more time to undergo both processes. Second, the process requires some transport of the O atoms to reach large densities of O_2. By 50 μs, the gas that was originally in the middle of the tube has reached the tube exit. At this time, O atoms formed by dissociation of oxygen inside the tube come into contact with the humid air which greatly increases the rate of O_3 formation. Using molecular beam mass spectrometry, van Ham *et al* reported that O_3 did not have a significant density until 1 cm downstream of the APPJ [31]. The O_3 densities of 3×10^{13} cm^{-3} measured in this experiment are consistent with the densities predicted by the model in spite of the larger energy deposition.

The density of OH peaks at 2×10^{13} cm^{-3} at the interface of the He and the air immediately outside the tube at 21 μs. This localized OH production corresponds to the region of high rates of photoionization. In this region VUV photons ionize N_2, forming N_2^+ which then charge exchanges with H_2O. OH is then produced by the formation of hydronium, $H_2O^+ + H_2O \rightarrow OH + H_3O^+$. More OH is produced inside the tube than O, due to the H_2O impurities having a higher concentration than O_2 and a larger cross section for electron impact dissociation compared to O_2. OH later combines to form H_2O_2 in the gas phase, but the reaction occurs more rapidly on surfaces. Measurements of OH densities 1 mm outside of a radio frequency powered APPJ showed densities of 8×10^{13} cm^{-3}, which is larger than that predicted here (6×10^{12} cm^{-3}) due to a higher average specific energy deposition [32]. LIF measurements of OH densities outside of a pure He 8 kHz pulsed APPJ were approximately 5×10^{13} cm^{-3} for 9 kV at 1 μs after the plasma pulse, which is larger than the value calculated here. The larger densities in the experiment are due to a larger energy deposition outside of the tube that likely occurs with a longer pulse duration as well as some accumulation of OH from one pulse to the next [19].

HO_2 is generated from H atoms, produced from dissociation of water, reacting with O_2 in the air, reaching a peak density of 2×10^{13} cm^{-3}. After 150 μs, HO_2 densities decrease due to reactions with itself ($HO_2 + HO_2 \rightarrow H_2O_2 + O_2$), and its consumption in forming RNS, primarily by the reactions $HO_2 + NO \rightarrow HNO_3$ and $HO_2 + NO \rightarrow ONOOH$.

The densities of RNS in figure 6(b) are shown at the time when their individual densities are maximum. N is initially produced inside the tube by dissociative recombination of electrons and N_2^+, the latter produced by electron impact ionization, charge exchange from He$^+$, and Penning ionization of the impurity N_2. NO forms outside the tube dominantly by $N^* + O_2 \rightarrow NO + O^*$, reaching a peak density of 5×10^{12} cm^{-3} after 61 μs. When operating at high frequency, RONS can accumulate on a pulse-to-pulse basis. This is demonstrated by the results of molecular beam mass spectrometry of the average NO density for an Ar APPJ operating at 13.56 MHz which are a factor of 20 larger than the single pulse, low frequency density predicted here due to the accumulation from successive pulses that occurs at high frequency [31]. Once NO forms, it can react with ROS (OH, HO_2, O, H) to form more complex NO_x and HNO_x. The more complex RNS tend to form later in time due to the several reaction steps required for their formation. The density of NO_2 peaks at 4×10^{10} cm^{-3} after 180 μs, and it is primarily produced by $NO + HO_2 + M \rightarrow NO_2 + OH$ and $NO + O + M \rightarrow NO_2 + M$. Since NO_2 is produced by reactions between multiple RONS, which are at lower densities (10^{12}–10^{13} cm^{-3}) than the background air, NO_2 is produced later than either N or NO. HNO_x represents the sum of HNO_2, HNO_3, and ONOOH. It is the final state of RNS with the longest lifetime in this mechanism in the absence of organic species with which the species could react. The total density of HNO_x, peaks at 3×10^{11} cm^{-3} at 220 μs. This density is comprised of 5×10^{9} cm^{-3} HNO_2, 1×10^{11} cm^{-3} HNO_3, and 2×10^{11} cm^{-3} ONOOH. The total inventory of HNO_x continues to rise until the plume of RONS reaches the pump, however convective and diffusive transport disperses HNO_x, lowering its peak density.

3.2. Coaxial ground

The location of the electrical ground outside the APPJ is important to the production of RONS due to the sensitivity of the IW to electrostatic coupling to ground. Computationally, this occurs through solution of Poisson's equation where the metal ground is a boundary condition having zero potential. From a circuit perspective, a ground plane is the return path for current produced in the plasma. This current is dominantly displacement current for the coaxial ground and may contain conduction current for the ground represented by the pump port. The location of electrical ground is often not mentioned in reports of experimental studies, which may imply that the location of ground is not being controlled. As a result, replicating the experimental result could be difficult. In this study, the radius of the coaxial ground was varied to examine the sensitivity of the plasma properties and RONS production. The propagation of the IW, shown by the electron density in figure 7, changes significantly as the radius of the coaxial ground is increased from 0.4 to 5.4 cm. With a closer coaxial ground, the radial electric fields at the surface of the electrode are larger and so the IW is more intense (higher S_e). The resulting plasma is also more annular, resulting in larger energy deposition in areas where the He is in direct contact with the air. The total capacitance seen by the plasma, C_{tot} can be approximated by two coaxial annular capacitors:

$$\frac{1}{C_{\text{tot}}} = \frac{1}{C_t} + \frac{1}{C_a}, \tag{15}$$

where C_t, the capacitance of the dielectric tube, and C_a, the capacitance of the ambient air in the gap between the tube and the coaxial ground, are added as capacitors in series. In terms of capacitance per unit length:

$$\frac{C_t}{L} = \frac{2\pi\varepsilon_{\text{r}}\varepsilon_0}{\ln\left(\frac{r_o}{r_i}\right)}, \tag{16}$$

where r_i and r_o are the inner and outer radii of the dielectric tube, and ε_r is the relative dielectric constant of the tube. The capacitance of the ambient space between the tube and the coaxial ground is similarly

$$\frac{C_a}{L} = \frac{2\pi\varepsilon_0}{\ln\left(\frac{r_g}{r_o}\right)}, \tag{17}$$

where r_g is the radius of the coaxial ground. As r_g increases, the capacitance decreases. C_{tot}/L is dominated by the smaller capacitance, which under usual circumstances would be C_a.

With this approximation, C_t/L varies from 2.5×10^{-13} F cm^{-1} to 1.2×10^{-13} F cm^{-1} as r_g increases from 0.4 cm to 5.4 cm. The charging of the inner wall of the tube by the plasma reflects this change in capacitance. The charge density at the surface of the tube at a height of 1 cm at 150 ns decreases in magnitude from -9.4×10^{-7} C cm^{-3} to -5.6×10^{-7} C cm^{-3} as r_g increases from 0.4 cm to 5.4 cm. For a given voltage, this capacitance is a measure of the maximum charge transfer by the plasma inside the tube. As a result, the total energy coupled to the plasma decreases from 40 μJ to 6.7 μJ with increasing radius of the coaxial ground for the same voltage pulse. A nearby coaxial ground plane increases the maximum charge transfer as well as the electric field. Therefore the total energy deposition (time integrated $\vec{j} \cdot \vec{E}$) increases by a factor of 6 when the capacitance increases by only a factor of 2.

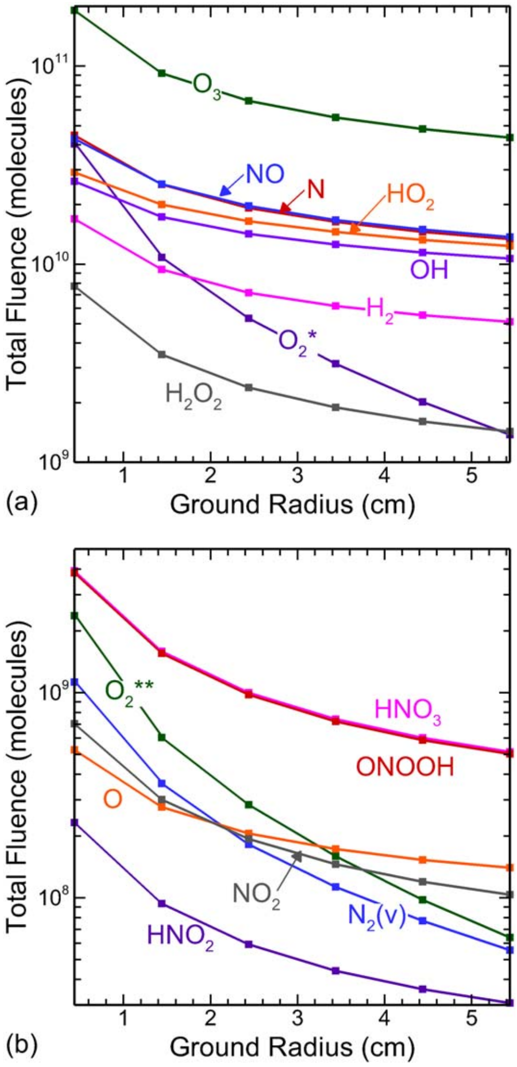

Figure 8. Plasma produced species as a function of the radius of the coaxial ground plane. The total fluence refers to the time and spatially integrated flux crossing the pump surface, or the total number of molecules which have exited the computational domain. (a) O_2^*, O_3, OH, H_2O_2, HO_2, H_2, N, and NO. (b) O_2^{**}, N_2(v), O, NO_2, HNO_2, HNO_3, and ONOOH.

To compare RONS production for different geometries and conditions, the fluxes of reactive species crossing the face of the pump were time integrated for 4 ms after the voltage pulse to produce a fluence as the gas flows out of the computational domain. This is enough time for all of the plasma produced species to be flushed out of the system for a single discharge pulse. Integrating the fluence over the area of the pump produces the total number of each species exiting the computational domain—or the total fluence of a species. This total fluence is not necessarily the same as the total production of individual RONS as some species are consumed between their site of production and reaching the pump. However, this total fluence is an indication of the reactive species that might, for example, reach a surface being treated.

The resulting total fluences of RONS as a function of radius of the coaxial ground are shown in figure 8. (Recall that the voltage pulse waveform is constant.) The total fluences of RONS have approximately a dependence of r^{-n} on the radius of the coaxial ground, where n varies from 0.3 to 1.1. This scaling corresponds to decreases in the total fluences by 57%–97% as the radius of the coaxial ground increases. In the case of O_3, the most abundant ROS, the total fluence from a single pulse decreases from 1.9×10^{11} molecules to 1.3×10^{10} molecules as the radius increases from 0.4 to 5.4 cm. The total fluences of excited states [O_2^* O_2^{**}, $N_2(v)$] which are dominantly formed by direct electron impact are the most sensitive to propagation of the IW outside the tube, and therefore the most sensitive to the location of the coaxial ground. The total fluences of these species drop by more than 95% as the radius of the ground increases. The species that are produced from reactions among several RONS are next most sensitive to the radius of the coaxial ground. These species include HNO_2, HNO_3, ONOOH, NO_2, and H_2O_2, whose total fluences decrease by 81%–87% as the radius increases.

As the radius of the coaxial ground plane increases with a constant voltage waveform, the energy deposition and the dissociation fraction decrease. This means that after an initial dissociation, with increasing radius a given molecule is more likely to react with background air compared to reacting with other RONS. The species that are formed following an initial dissociation and potentially followed by reaction with the background air are least sensitive to the radius of the ground, and include O_3, O, N, NO, OH, and HO_2. The total fluences for these species decrease by 57%–77% as the radius of the coaxial ground increases. These species still decrease with increasing radius of the ground as the energy deposition decreases, however, not as severely as the prior two groups of species. This reduced sensitivity is due to these species not being exclusively produced outside of the tube or being generated by successive reactions among RONS. For example, in the case of a close coaxial ground, the energy deposition is high and an OH radical formed by dissociation of H_2O is likely to react with another OH to form H_2O_2. However, if the ground plane is distant with less energy deposition, the density of OH is lower, and the OH is more likely to reach the pump before reacting with another OH. This results in the total fluence of H_2O_2 being sensitive to ground plane placement because its formation scales with the square of the OH density.

The exception to this group of less sensitive species is H_2, with a total fluence which decreases by only 70% in spite requiring a reaction between radicals ($H + H + M \rightarrow H_2 + M$). As the coaxial ground plane is moved closer to the tube, there is greater dissociation of molecules in the tube and more interaction between plasma produced species. The reaction $O + H + M \rightarrow OH + M$, depletes the H available for H_2 formation, which occurs approximately a factor of 4 slower. This translates to H_2 formation being less sensitive to the location of the coaxial ground because of the competition for H from other reactions.

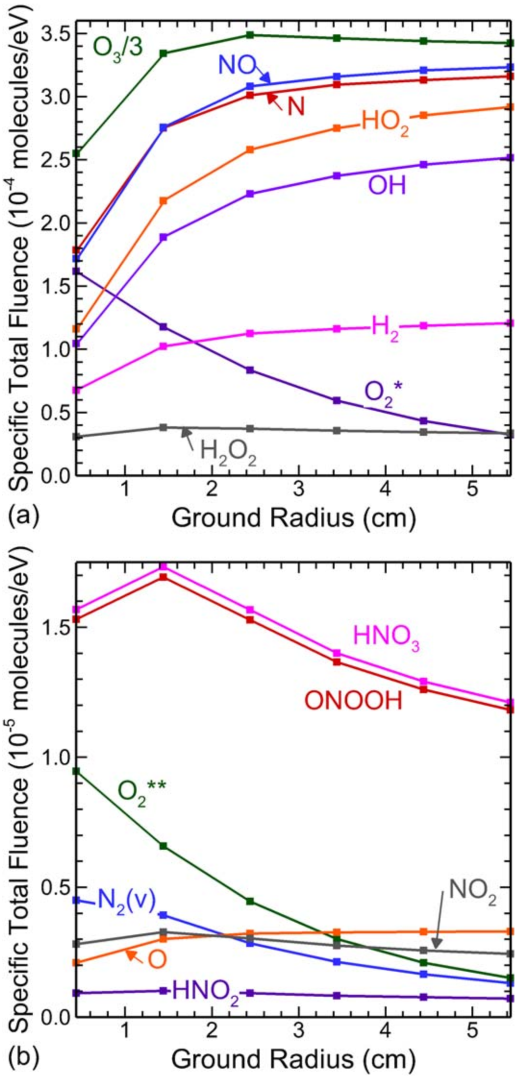

Figure 9. Total fluence of species per eV of energy deposition (specific total fluence) as a function of radius of the coaxial ground. The total fluence is the time and spatially integrated flux crossing the pump surface. (a) O_2^*, O_3, OH, H_2O_2, HO_2, H_2, N, and NO. (b) O_2^{**}, $N_2(v)$, O, NO_2, HNO_2, HNO_3, and ONOOH.

APPJs can be operated in a constant voltage (as in the previous examples) or a constant power (or energy/pulse) mode. Since the total energy deposition changes with the radius of the coaxial ground, part of the change in the total fluence of RONS is a consequence of the change in energy deposition and not necessarily due to a change in the structure of the discharge. To deemphasize variations due to energy deposition, total fluences were normalized by the energy deposition per pulse. The resulting total fluences, expressed as molecules-eV^{-1} (called the specific total fluence), are shown in figure 9. The dependence of the specific total fluence on radius of the coaxial ground has less variation than the raw total fluences. The specific total fluences as a function of radius can be parsed into the same groups. The specific total fluences for O_2^*, O_2^{**} and $N_2(v)$, decrease monotonically as the ground radius is increased. These species are particularly sensitive to IW propagation outside of the tube. As the radius of the coaxial ground increases, the IW is slower and less energy is deposited outside of the tube. The species that require interaction between multiple RONS generally have specific total fluences that decrease with increasing ground radius. At small radius, there is a higher dissociation fraction, enabling the RONS to interact with each other to a greater

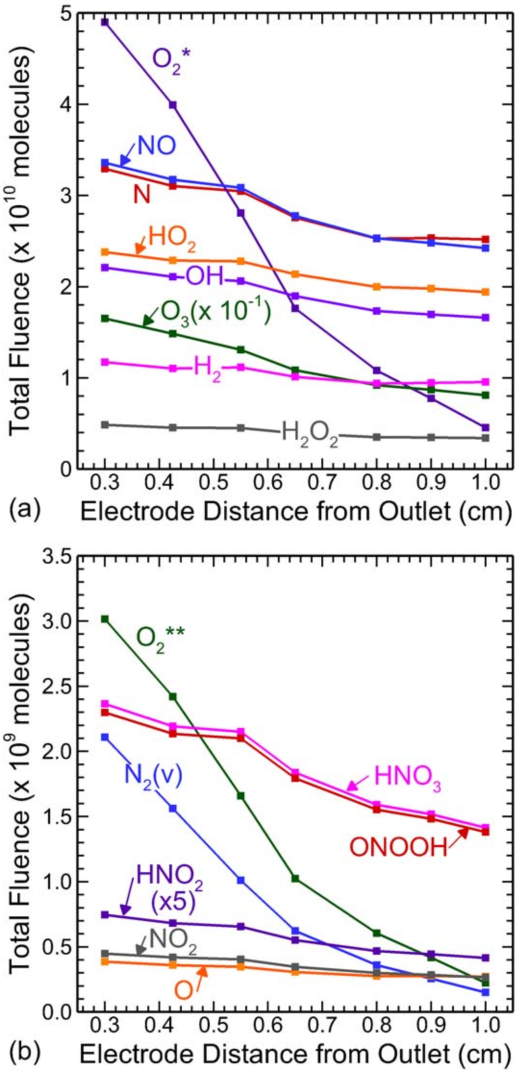

Figure 10. The total fluence of plasma produced species as a function of distance of the powered electrode from tube outlet for a jet with a single powered ring electrode. The total fluence is the fluence integrated across the pump outlet surface, resulting in units of molecules. (a) O_2^*, O_3, OH, H_2O_2, HO_2, H_2, N, and NO. (b) O_2^{**}, N_2(v), O, NO_2, HNO_2, HNO_3, and ONOOH.

degree. The species which require an initial dissociation or excitation followed by a reaction with the ambient air have specific total fluences which increase with increasing ground radius (or decreasing energy)—meaning more efficient production. Generally, at lower total energy, the production of reactive species is more efficient.

In this study the ground plane is cylindrically symmetric about the jet axis, which would likely not be the case for coincidental grounds in the vicinity of the jet. It is reasonable to expect that these asymmetric grounds could lead to asymmetries in the plasma.

3.3. Electrode position

Even with a well-controlled coaxial ground, the placement of the single powered electrode along the axis of the tube will affect RONS production. To investigate this sensitivity, the powered electrode was moved from 3 mm from the end of the tube to 10 mm, with the coaxial ground fixed at a radius of 1.4 cm. (Again, the voltage waveform is first held constant.) The total fluences of species exiting the computational domain as a function of position of the electrode are shown in figure 10. Placing the powered electrode further from the end of the tube results in the IW exiting the tube later during the voltage pulse, thereby depositing less energy outside of the tube in the ambient air environment. The end result is decreasing RONS production. The total energy deposition also decreases as the electrode is moved further from the end of the tube. The time for the IW to reach the end of the tube increases from 19 ns to 106 ns as the electrode is moved from 3 to 10 mm from the end of the tube. With this shift in the electrode, the total energy deposition decreases from 28.1 μJ to 13.6 μJ, and the fraction of energy deposited outside the tube decreases from 18.3% to 2.3%. The distance that the IW propagates past the end of the tube decreases as the electrode is moved further from the end of the tube. This trend is consistent with experimental observations by Maletic *et al*, although these studies were performed with a different electrode configuration having a grounded ring [18]. Recall that a less intense IW also propagates backwards from the ring electrode towards the He nozzle, and this IW also contributes to radical production which is also eventually blown out of the tube.

The species with total fluences that are most sensitive to the electrode placement are O_2^*, O_2^{**}, and N_2(v), decreasing by 90%–93% as the powered electrode is moved away from the outlet. These species are initially produced by electron impact excitation, and eventually they collisionally de-excite. Their production occurs primarily outside of the tube where the air concentration is highest. Electron impact rate coefficients for production of these species are less sensitive to the decrease in T_e outside the tube ($\leqslant$2 eV), as excitation of these species have relatively low threshold energies (0.3, 1.0, and 1.6 eV for N_2(v), O_2^*, and O_2^{**}). As a result, their production is sensitive to the propagation of the IW outside of the tube. When the electrode is further from the end of the tube, the IW does not propagate as far outside of the tube into regions of higher air concentration, and less O_2^*, O_2^{**} and N_2(v) are produced, facilitated by energy deposition outside of the tube decreasing from 5.1 μJ to 0.3 μJ.

O_3, O, H_2O_2, NO_2, HNO_2, HNO_3, and ONOOH are moderately sensitive to the position of the electrode, with total fluences that decrease by 30%–51% as the electrode is moved from 3 mm to 10 mm from the outlet. O_3 is sensitive because the amount of O generated is nearly a linear function of the total energy deposition in the plasma, which increases as the electrode is moved closer to the outlet. This O is converted to O_3 by reaction with humid air on timescales of $\sim$100 μs. The initial OH production is moderately sensitive to the electrode placement, and the OH is eventually converted to H_2O_2, making the H_2O_2 moderately sensitive. The total fluence of OH itself is less sensitive to electrode placement, because producing more OH increases H_2O_2 production, which depletes the OH total fluence by the time the RONS reach the pump.

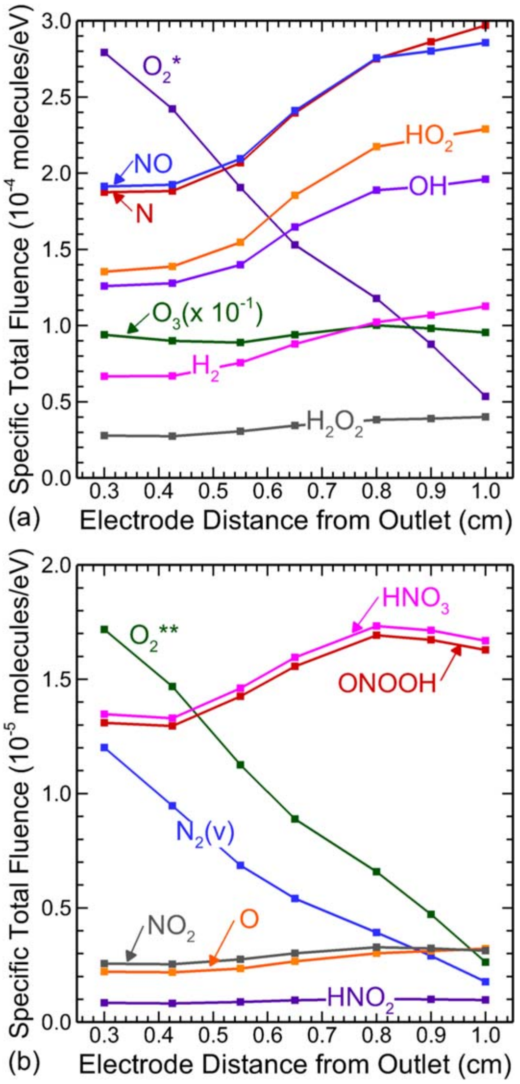

Figure 11. The total fluence of species per eV of energy deposition (specific total fluence) as a function of distance of the powered electrode from tube outlet for a jet with a single powered ring electrode. Electrodes close to the outlet lead to a higher energy deposition and less energy efficient production. (a) O_2^*, O_3, OH, H_2O_2, HO_2, H_2, N, and NO. (b) O_2^{**}, N_2(v), O, NO_2, HNO_2, HNO_3, and ONOOH.

NO_2 production is primarily by the reaction of NO with O or HO_2, requiring reactions between multiple plasma produced RONS. Since all RONS decrease as the electrode is moved further from the outlet and NO_2 is at least second order in overall RONS production, the decrease in the total fluence of NO_2 is more sensitive to the electrode moving further from the end of the tube. The more significant decreases in total fluences of HNO_2, HNO_3 and ONOOH as the electrode moves away from the outlet are also due to their requiring reactions between multiple RONS. For example, HNO_3 is primarily produced by NO + HO_2 → HNO_3, so this is at least second order with respect to RONS production.

NO, OH, N, H_2, and HO_2 are least sensitive to electrode placement, with total fluences decreasing by 18%–28% as the electrode is moved from 3 mm to 10 mm from the outlet. The production of N predominantly originates inside the tube near the powered electrode, being produced in the afterglow by dissociative recombination, $e + N_2^+ \rightarrow N + N^*$. Since N is primarily produced inside the tube, its total fluence is not sensitive to propagation of the IW outside of the tube, and therefore not very sensitive to electrode position. The total fluence of N does decrease by 24% with electrode position because the energy deposition inside the tube increases. NO largely originates from the N^* produced inside or outside of the tube reacting with O_2. The N^* produced in the tube is the more significant source, and as a result the NO only varies by 28% as the electrode is moved from 3 mm to 10 mm from the end of the tube. Initial OH production decreases by 30% as the electrode is moved away from the end of the tube, however, the total OH fluence collected at the pump decreases by only 25%. This decrease in sensitivity is a consequence of larger production of OH being more rapidly converted to H_2O_2. H is primarily produced inside of the tube, and H is consumed in making HO_2, H_2 and OH. The total fluences of these stable species are least sensitive to the electrode position, varying by only 18% over the electrode positions studied.

The specific total fluences as the distance between the electrode and the end of the tube is increased are shown in figure 11. The specific total fluences decrease by 81%–84% for N_2(v), O_2^*, and O_2^{**} as the electrode is moved further from the end of the tube. These species are dominantly produced outside of the tube in regions of high air concentration, and so their densities decrease as the fraction of energy deposited outside of the tube decreases. This occurs when the electrode is moved further from the end of the tube.

All of the other species have specific total fluences that increase as the electrode is moved away from the end of the tube. This trend results in configurations producing higher energy deposition in the plasma (e.g., electrode closer to the end of the tube) being less efficient at producing RONS while the total fluence of RONS is larger. Species that are primarily produced from energy deposition inside the tube, including HO_2, H_2, N, OH and NO, have specific total fluences which increase by 48%–69% as the electrode moves further from the end of the tube. Recall that the fraction of energy deposited outside of the tube decreases from 18.3% to 2.3% when moving the electrode further from the end. The energy deposited outside of the tube is significantly less efficient at producing HO_2, H_2, N, OH, and NO. The electron temperature T_e is lower outside of the tube, and with a larger mole fraction of molecular species a larger fraction of the energy deposition occurs by vibrational and rotational excitation which have low threshold energies. These processes primarily result in gas heating and produce little reactive chemistry.

O, H_2O_2, NO_2, and HNO_x have specific total fluences which increase by 15%–46% as the electrode is moved away from the end of the tube. H_2O_2, NO_2, and HNO_x require reactions between multiple RONS, and therefore their production is favored at higher energy deposition (when the electrode is closer to the outlet). Although the efficiency of their production is lower when the electrode is near the outlet, this effect is mitigated by the increase in rates of reaction among the larger densities of RONS that are produced. The

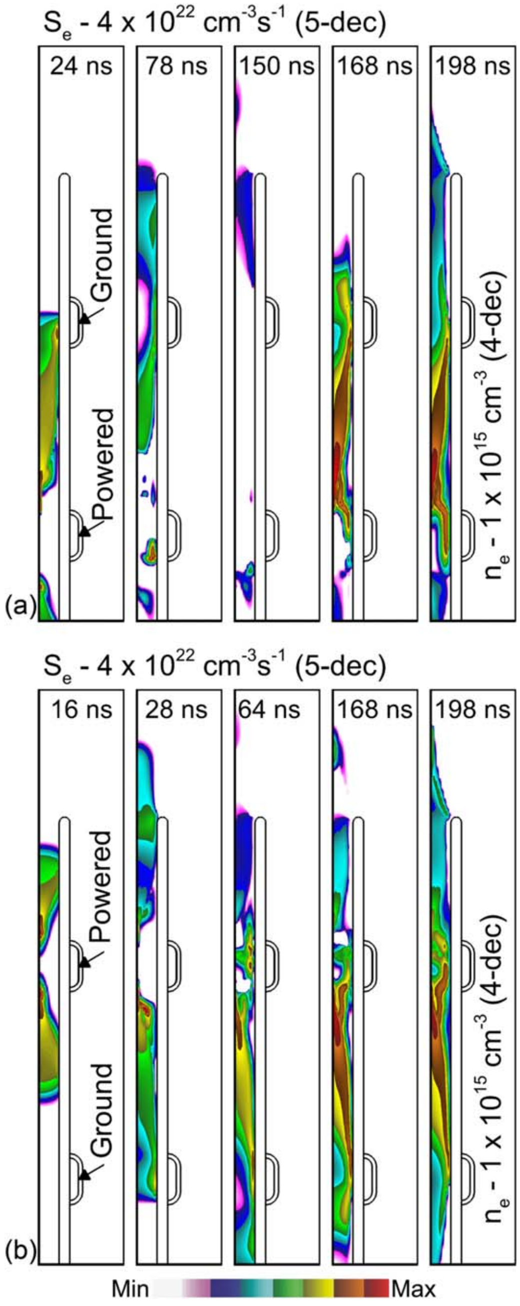

Figure 12. Ionization wave propagation for a two-ring electrode jet. The left four frames show the electron impact ionization source term (S_e) on a five-decade log scale. The rightmost frame shows the electron density (n_e) on a four-decade log scale. (a) The ground electrode is closer to the outlet. The plasma is more concentrated between the two electrodes where the electric field is initially highest. (b) The powered electrode is closer to the outlet. The plasma is most intense between the two electrodes, but the ionization wave does rapidly exit the tube producing significant ionization where the He meets the air.

specific total fluence of O_3 is unexpectedly almost independent of electrode placement, varying by only 1.5%. This result suggests that regardless of where the energy is deposited, the efficiency of producing O is nearly the same, and that the lifetime of O is long enough to form O_3 by collisions with O_2 before reacting with other species.

3.4. Grounded ring electrode

Adding a grounded ring electrode around the tube produces a higher electric field between the powered electrode and the grounded ring. For example, the IW in a jet with a grounded ring separated from the powered electrode by 4 mm is shown in figure 12(a). The IW traveling between the powered and grounded ring has an average speed of 2.7×10^7 cm s^{-1} which is 43% faster than in the base case. The IW is also volumetric (as opposed to surface-hugging). Upon reaching the grounded ring, the IW slows to 6.9×10^6 cm s^{-1}, as the IW charges the higher capacitance at the location of the grounded ring electrode. During this time, the electron density in the volume between the electrodes increases from 2×10^{12} cm^{-3} to 6×10^{12} cm^{-3}. After passing the grounded electrode, the IW becomes more annular, shifting from a volume IW to a SIW. The end result is an increase in energy deposition in the tube by a factor of 9 compared to the base case, and a decrease in energy deposited outside of the tube, which is reflected in the electron density shown in figure 12(a). Yue *et al* experimentally observed a factor of 5 increase in energy deposition with the addition of a grounded ring, which is consistent with the modeling results [19]. With the grounded ring electrode, the IW in the model reaches the end of the tube 8 ns earlier than in the base case in spite of E/N and T_e being lower—$T_e = 3.6$ eV for the base case compared to 3.2 eV with the grounded ring. With the proximity of ground provided by the ring electrode, the capacitance of the tube is larger which results in more charging of the tube. The larger charge shields out the applied voltage resulting in the IW not extending as far into the ambient. With more energy deposition in the tube, the electron density between the electrodes increases from 9×10^{12} cm^{-3} in the base case to 1×10^{14} cm^{-3} with the grounded ring. This increase in electron density inside the tube comes at the cost of a reduction in electron density outside the tube, from 4×10^{12} cm^{-3} for the base case to 2×10^{12} cm^{-3} with the ring electrode.

In the next configuration, shown in figure 12(b), the powered and grounded ring electrodes are switched. Placing the powered electrode closer to the outlet also produces a reverse IW (propagating opposite the direction of He flow) that is more intense than the IW exiting the tube. This configuration also produces an electric field that is larger inside the tube between the electrodes, and weaker in the direction of the tube exit. The two counter-propagating IWs are initially comparable in magnitude of the ionization source S_e and speed. However, as the reverse IW approaches the grounded ring, the peak value of S_e and speed increase. At 18 ns, S_e for the forward IW is 3×10^{20} cm^{-3} s^{-1}, while it is 2×10^{21} cm^{-3} s^{-1} for the reverse IW approaching the grounded electrode. The electron density at the end of the pulse is highest between the electrodes, as shown in figure 12(b), reaching 6×10^{14} cm^{-3}. The IW outside of the tube is more intense compared to having the grounded electrode close to the exit (figure 12(a)), producing an electron density of 4×10^{13} cm^{-3}, a factor of 10 higher than the base case, and a factor of 5 higher than having the grounded ring close to the

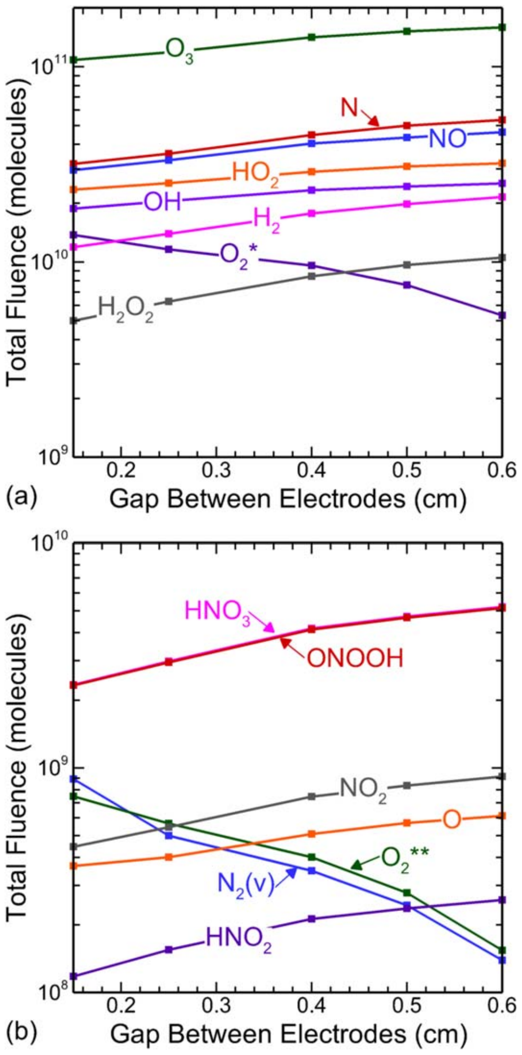

Figure 13. The total fluence of species exiting the computational domain for jets with two ring electrodes as a function of the gap between the electrodes. The grounded ring electrode is fixed on the top (as in figure 12(a)), the position of the powered electrode was varied from 1.5 to 6 mm from the ground electrode. (a) $O_2{}^*$, O_3, OH, H_2O_2, HO_2, H_2, N, and NO. (b) $O_2{}^{**}$, $N_2(v)$, O, NO_2, HNO_2, HNO_3, and ONOOH.

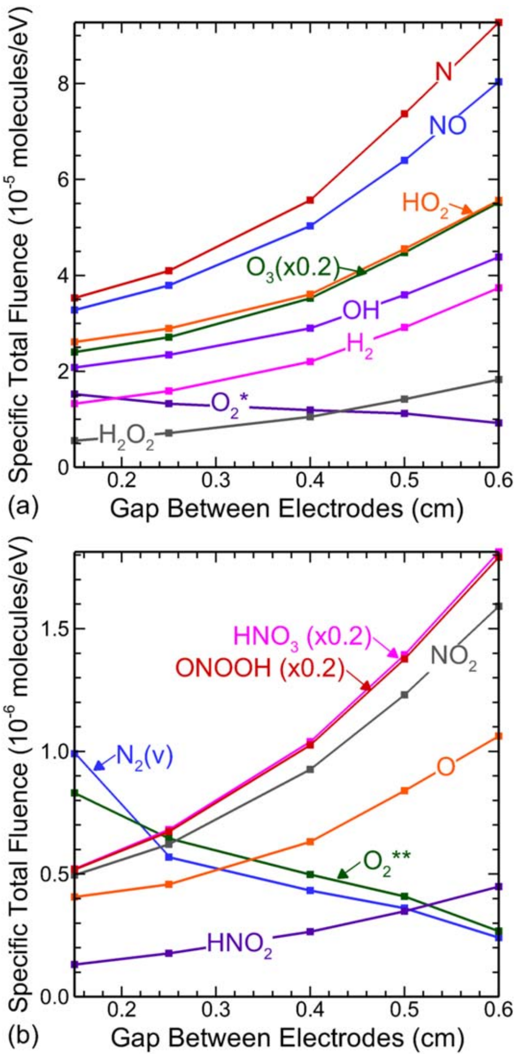

Figure 14. The total fluence of species per eV of energy deposition (specific total fluence) for jets with two ring electrodes as a function of the gap between the electrodes. The grounded ring electrode is fixed on the top (as in figure 12(a)), the position of the powered electrode was varied. As this gap is increased, the energy deposition decreases and the energy efficiency increases. (a) $O_2{}^*$, O_3, OH, H_2O_2, HO_2, H_2, N, and NO. (b) $O_2{}^{**}$, $N_2(v)$, O, NO_2, HNO_2, HNO_3, and ONOOH.

exit. The effects of these configurations on RONS production are compared to the base case in section 3.7.

3.5. Electrode gap

In the configuration having a powered ring electrode on the bottom and grounded ring electrode on the top (as in figure 12(a)), the position of the powered electrode was varied from 1.5 mm to 6 mm from the ground electrode. The resulting total fluences of plasma produced species are shown in figure 13. The total fluences of reactive species vary by approximately a factor of 3. The total energy deposition decreased from 144 μJ to 92 μJ as the gap between the electrodes increased. The increasing gap reduced the electric field between the electrodes, resulting in a slower and less intense IW, reducing T_e in the IW from 6.5 eV to 6.1 eV, and delaying the time the IW exits the tube by 64 ns. The later exit is in large part due to the powered electrode moving further from the tube outlet.

With the electrode gap increasing, the energy deposition decreases and the propagation of the IW outside of the tube decreases while the volume of plasma between the electrodes increases. The end result is that the total fluences of electronically and vibrationally excited states disproportionately decrease—lower total energy deposition with a smaller fraction outside the tube, producing a lower n_e outside where the majority of the $N_2(v)$, $O_2{}^*$ and $O_2{}^{**}$ are produced. Other RONS have total fluences which increase with the gap between the electrodes and are all less sensitive to gap separation. The more complex species, which require reactions between several RONS, are moderately sensitive to gap separation. These species include ONOOH, HNO_3, HNO_2,

H_2O_2, NO_2, and H_2. Though the plasma density and energy deposition are lower with a larger gap, the plasma volume is also larger. As a result, the total inventory (volume integrated number density) of electrons and nearly all of the reactive species increase with increasing gap. With the higher power density for the shorter gap, the impurities of N_2, O_2, and H_2O are depleted by up to 30%, thereby decreasing the production rate of RONS in the region of highest energy deposition.

The specific total fluences are shown in figure 14 as a function of the gap between the ring electrodes. Smaller gaps produce higher energy deposition and lower production of most species, making these configurations significantly less efficient for generating most species compared to larger gaps. The exceptions to this trend are O_2^*, O_2^{**}, and $N_2(v)$, due to their sensitivity to IW propagation into volumes of high air concentration. As the gap is increased, the distance from the powered electrode to the end of the tube increases, and there is less propagation of the IW outside of the tube. Overall, although placing the electrodes further apart decreases the energy coupled to the plasma, for the range of gap investigated RONS production increased.

3.6. Powered electrode inside the tube

Placing an annular powered electrode inside the tube eliminates the charging of the inner surface of the tube at the powered electrode—that is, there is no longer a capacitor between the plasma and the high voltage electrode which would both limit current and shield voltage. Two ground ring placements were compared using an internal, powered annular electrode—8 mm (figure 15(a)), and 3 mm (figure 15(b)) from the powered electrode. Both cases display similar qualitative behavior, however the placement of the grounded electrode affects the timescales of the dynamics. With an 8 mm gap between the electrodes, the IW begins at the powered electrode, and propagates toward the grounded ring with a high speed (1×10^7 cm s^{-1}), and an intensity on the order of the base case (1×10^{19} cm^{-3} s^{-1}). Upon reaching the grounded electrode, the IW slows to 5×10^6 cm s^{-1}. After passing the grounded electrode, the IW becomes more annular resembling a SIW, and its speed increases back to 1×10^7 cm s^{-1}. The energy deposition is 346 μJ, significantly higher than in other cases previously discussed. This higher energy deposition is enabled by current to the powered electrode not being limited by charging of an intervening dielectric.

With the grounded ring 3 mm from the powered electrode, the IW propagates faster between the electrodes by a factor of 3 (3×10^7 cm s^{-1}). Upon reaching the grounded electrode, the IW slows to 1×10^7 cm s^{-1}. After passing the grounded ring the speed returns to 3×10^7 cm s^{-1}. As a result, the IW reaches the exit of the tube at 54 ns, compared to 102 ns for the more distant ground. The total energy deposition of 405 μJ is also higher. Placing a grounded electrode close to the powered electrode enables more energy

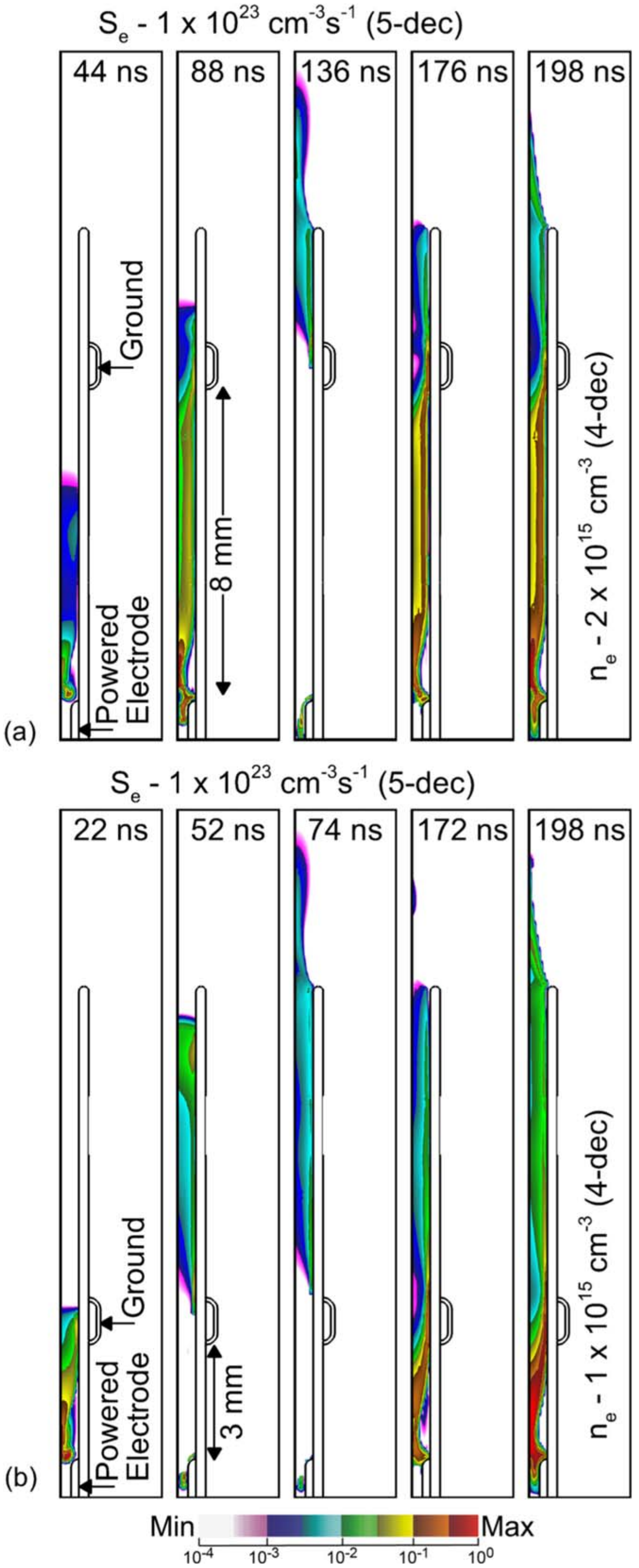

Figure 15. Ionization wave behavior with the powered ring electrode inside the tube and the grounded ring outside of the tube. The left four frames are the electron impact ionization source term, S_e, on a five-decade log scale, and the rightmost frame is the electron density, n_e, on a four-decade log scale. (a) Ground electrode is 8 mm and (b) 3 mm from the powered electrode.

to be deposited outside of the tube (9 μJ compared to 5 μJ), though this is not a large fraction of the total energy deposition. Moving the grounded ring further from the powered electrode (and closer to the tube outlet) allows a larger fraction of the energy to be deposited inside of the tube. These trends may be useful for tailoring the reactive species production by controlling the location of energy deposition.

APPJs with similar electrode configurations have been investigated in several experiments. Electron densities and temperatures were measured by Klarenaar *et al*, in an APPJ having a 5 mm gap between the electrodes [33]. As the IW passed 2 mm from the outlet of the tube, measurements showed $T_e = 3$ eV and $n_e = 3 \times 10^{12}$ cm^{-3}. In the simulation, as shown in figure 15(a), T_e at this point is marginally higher, 3.5 eV, possibly due to a higher applied voltage, and n_e is in agreement with the experiment. The electric field in this jet was measured to be 5–15 kV cm^{-1}, which is commensurate to but lower than the electric field calculated outside the tube in this work (12–17 kV cm^{-1}) due the lower applied voltage [34].

3.7. Reactive species generation

RONS production with the electrode configurations already discussed are compared with the base case in this section. Changing the electrode configuration can significantly change the energy deposition for a given applied voltage. In a given configuration, increasing the energy deposition usually increases RONS production and so efficiency should also be compared. Energy deposition is the largest for the jets with the powered electrode directly exposed to the plasma, 346 μJ–405 μJ, as shown in figure 16(a). This is due to there being no dielectric barrier between the powered electrode and the plasma, a barrier which can charge, screen out the applied voltage and limit current. The two-external ring configurations have a moderate energy deposition, about half that of the exposed electrode. The single ring electrode configurations have the lowest energy depositions of 15 μJ –28 μJ.

The ROS having the largest total fluences are shown in figure 16(b) and the RNS in figure 16(c). These total fluences are again the time and area integrated fluxes over the surface of the pump to represent the total number of molecules flowing out of the computational domain. To highlight trends in selectivity, the resulting total fluences for each species were normalized by values for the base case. Generally, the production of RONS tends to increase with the increasing energy deposition, though not linearly in each case. For example, with the center powered electrode, the total fluence of O_3 increases by only a factor of 4.2 from the base case while the energy deposition increases by a factor of 28. Moving the single powered electrode closer to the end of the tube increases all RONS for the reasons discussed in section 3.3.

First the consequences of adding a grounded ring to the base case will be discussed. This change in electrode configuration increases energy deposition but does not equally affect the production of all species. The increase in energy deposition is dominantly inside the tube between the

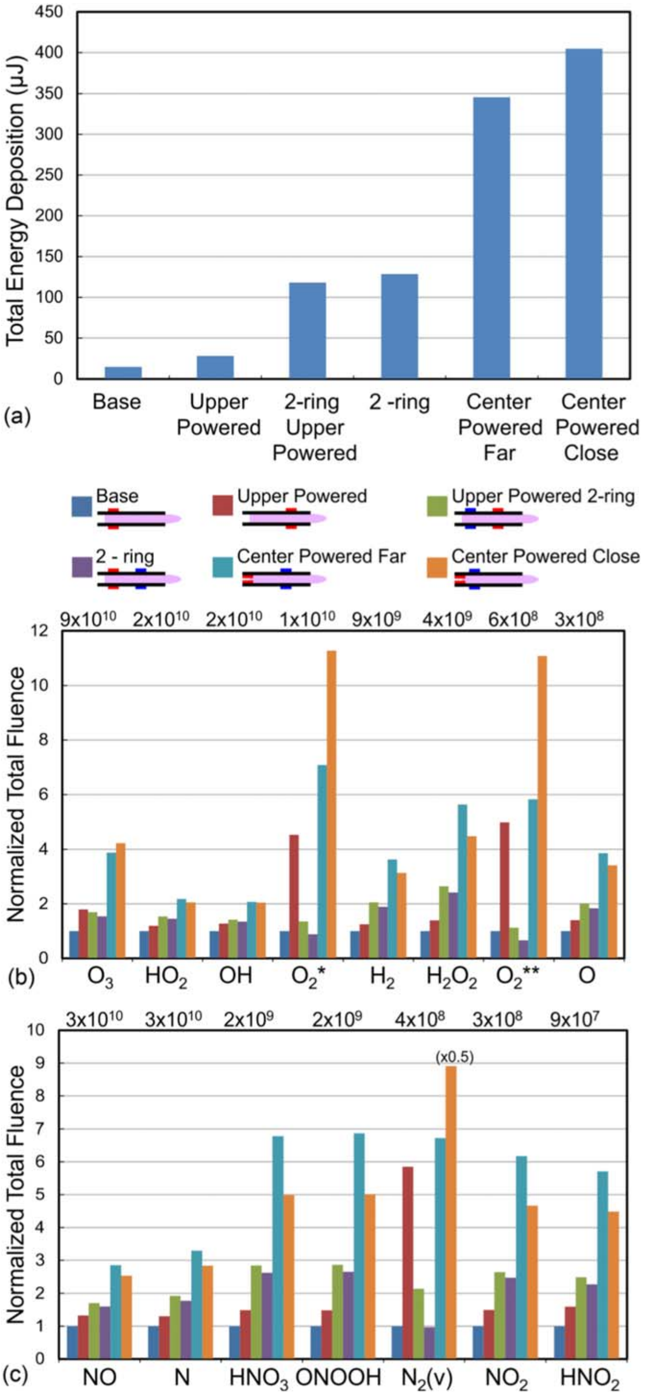

Figure 16. Comparisons of energy and total fluences between different electrode configurations. In each schematic, red indicates a powered electrode, and blue indicates a grounded electrode. The configurations are 'Base' (single ring electrode 8 mm from outlet, figure 3), 'Upper Powered' (single ring electrode 3 mm from the outlet), 'Upper Powered 2-ring' (two ring electrodes with powered on top, figures 12(b)), '2-ring' (two ring electrodes with powered on bottom, figure 12(a)), 'Center Powered Far' (internal electrode with large gap to ground, figure 15(a)), and 'Center Powered Close' (internal electrode with small gap to ground, figure 15(b)). (a) Volume integrated energy deposition ($\vec{j} \cdot \vec{E}$). The normalized total fluence of (b) species which do not contain nitrogen and (c) the nitrogen containing species. These values are normalized to the base case total fluence whose value in molecules is listed.

electrodes (as opposed to outside the tube). The RONS that take one or two steps to form (O_3, HO_2, OH, O, NO, N), are least sensitive to this increase in energy, increasing in total fluence by less than 80% in spite of energy deposition increasing by more than a factor of 4. Production of these species does not require reactions between multiple plasma-produced species or radicals. Each requires an initial dissociation or excitation, possibly followed by a reaction with the background gas. For example,

$$O + O_2 + M \rightarrow O_3 + M, \tag{18}$$

$$H + O_2 + M \rightarrow HO_2 + M, \tag{19}$$

$$N^* + O_2 \rightarrow NO + O^*. \tag{20}$$

Each of these reactions occurs rapidly in volumes having higher air concentration.

The OH total fluence increases by 35% when a grounded ring is added, which is consistent with measurements by Yue *et al,* which show an 14%–80% increase in OH densities when a grounded ring is added [19]. Yonemori and Ono also measured the OH and O densities in a pulsed He APPJ with a powered and grounded ring electrode [35]. The O density measured by TALIF (two-photon absorption laser-induced fluorescence) on axis at the outlet was approximately 10^{14} cm^{-3}. This value is larger than the maximum density at this position calculated in this work of 2×10^{13} cm^{-3} because the gas residence time is much longer than the interpulse period in the experiment, so there is some accumulation of species. Despite this, the OH density of 6×10^{12} cm^{-3} on axis at the outlet is consistent with the modeling results of the maximum OH density of 8×10^{12} cm^{-3} at this position. The better agreement with experiment for OH is due to its shorter lifetime which is less sensitive to pulse-to-pulse accumulation. The spatial distributions observed in the experiment—with the maximum OH density on axis and the maximum O density in the mixing zone of the He with the surrounding air—are also consistent with the model.

Species that require reactions among plasma produced species, such as H_2, H_2O_2, HNO_3, ONOOH, NO_2, and HNO_2 are more sensitive to the addition of the grounded ring which produces most of the RONS between the electrodes inside the tube. The result is the RONS tend to more rapidly react with each other to produce higher order species.

A few species are overly sensitive to energy deposition outside of the tube, including O_2^*, O_2^{**}, and $N_2(v)$. Adding a grounded ring increases the total energy deposition, but the energy deposition outside of the tube decreases, resulting in a 3%–44% decrease in the production of these species. As a result, the total fluences of these species are significantly higher when the powered electrode is close to the outlet and there is no grounded ring.

When adding a grounded ring electrode to configurations with a powered ring electrode, most of the resulting trends are generally independent of the location of the powered electrode. Generally, the inventories of species that take only one or two steps to form increase slightly with the addition of a grounded ring, and the inventories of the more complex RONS have a more significant increase, and the inventories of excited states decrease. The inventories of the excited states are larger when the powered ring is closer to the exit than in the base case, and are more sensitive to the addition of grounded electrode, decreasing by as much as 77%. The inventory of O_3 also decreases with the addition of a grounded electrode. The production of O_3 requires a significant background density of O_2. With the upper powered electrode, most of the O atoms are produced at the interface between the He and the humid air, and so are rapidly converted to O_3. When a grounded ring is added, a significant amount of O is produced between the rings, which results in a long flow time to reach the ambient O_2, enabling O to recombine or react with other RONS (e.g., NO or H) that are generated by the He impurities inside the tube.

Moving the powered electrode inside the tube increases the energy deposition and the production of all RONS compared to both the single and two ring configurations. Again, some species increase more than others. The species most sensitive to moving the powered electrode inside the tube are O_2^*, O_2^{**}, and $N_2(v)$. In spite of the fraction of energy deposited outside the tube decreasing, the total amount of energy deposited outside the tube increases, which enables production of these species from interaction with humid air. Species which are more sensitive to moving the electrode inside include H_2O_2, HNO_3, ONOOH, NO_2, and HNO_2, which require reaction between multiple RONS. H_2 is less sensitive, which is inconsistent with the previous discussion as it should require reactions among plasma generated species to form. This counter-intuitive trend occurs because inside the tube other reactions which consume H also increase, including $O + H + M \rightarrow OH + M$.

Moving the grounded ring closer to the powered electrode inside the tube increases energy deposition by 17%, but actually decreases the production of most species. The exceptions to this trend are O_2^*, O_2^{**}, $N_2(v)$, and O_3 (to a lesser extent) as these species are more more likely to be produced outside of the tube at the He/air interface. With the ground electrode closer to the powered electrode, the IW is a factor of 3 faster and the energy deposited outside of the tube nearly doubles. The plasma density is the highest between the electrodes, and much of the increase in RONS production is a result of dissociation of the impurities in this region. Moving the grounded electrode closer to the powered electrode decreases the volume of this region, and the production of complex RONS becomes limited by depletion of the impurities. In the region of high plasma density between the electrodes, more than half of the impurities of H_2O, N_2, and O_2 are consumed by dissociation, meaning the production of RONS is beginning to be limited by depletion.

The specific total fluences (molecules-eV^{-1}) are shown in figure 17 for the various electrode configurations. The most energy efficient RONS production occurs in jets with the lowest energy deposition, a single ring electrode, with the least energy efficient being the center powered electrode having the largest energy deposition. When a grounded ring is added to either the base or upper powered ring configurations, the specific total fluence of all RONS decreases. O_2^*, O_2^{**}, and $N_2(v)$ have specific total fluences which decrease the

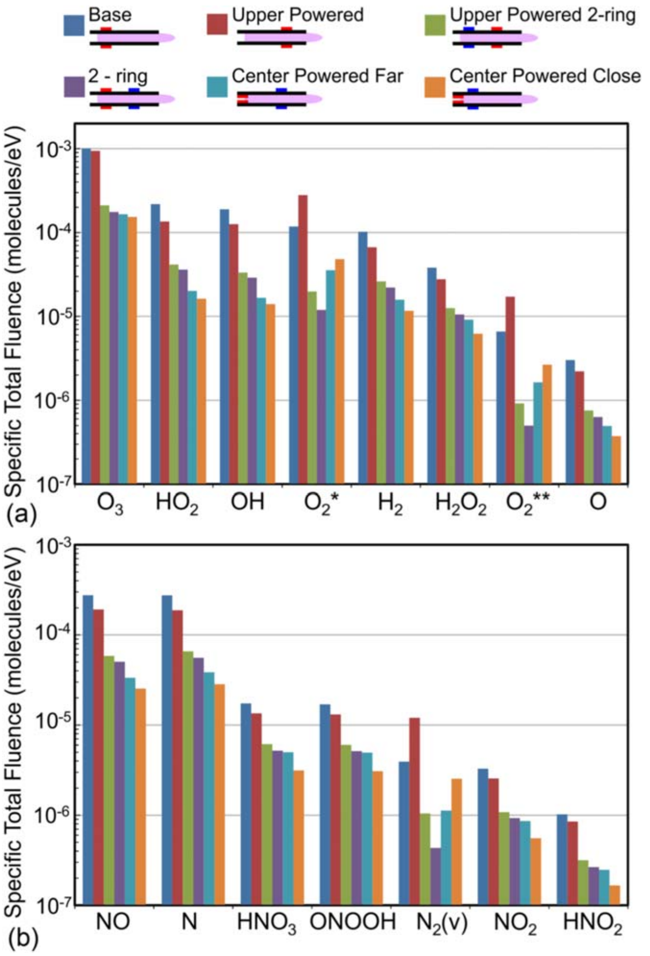

Figure 17. The total fluence of each species per eV of energy deposition (specific total fluence) for different electrode configurations. (a) Species which do not contain nitrogen and (b) nitrogen containing species. The descriptions of electrode placement are the same as in figure 16.

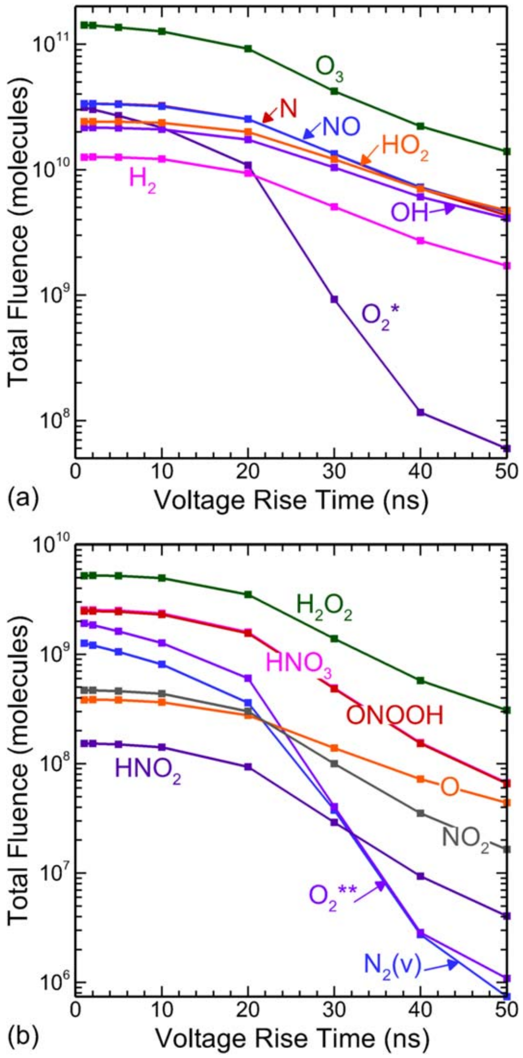

Figure 18. The total fluence of species exiting the computational domain as a function of the voltage rise time. Increasing the rise time leads to a slower ramp and slower ionization wave propagation. (a) O_2^*, O_3, OH, HO_2, H_2, N, and NO. (b) O_2^{**}, $N_2(v)$, O, H_2O_2, NO_2, HNO_2, HNO_3, and ONOOH.

most (more than 89%). The species which take one or two steps to form decrease by 65%–85% when a grounded ring is added. The more complex species, H_2, H_2O_2, HNO_3, ONOOH, NO_2, and HNO_2 have specific total fluences which only decrease by 54%–78%. When adding the grounded ring electrode, the additional energy deposition increases the dissociation fraction, and results in the RONS being more likely to react with each other.

3.8. Voltage rise time

The consequences of voltage rise time on total fluences of RONS for the single ring electrode (base case) geometry are shown in figure 18. Most of the total fluences scale similarly with voltage rise time—increasing the rise time from 1 ns to 50 ns generally produced about an order of magnitude reduction in total fluence. This effect is magnified by the relatively short duration of the voltage pulse, 170 ns. A longer rise time means that the applied voltage is at its maximum magnitude for a smaller fraction of the pulse. As a result, increasing the voltage rise time from 1 ns to 50 ns decreases the total energy deposition from 22 μJ to 2 μJ. In the case of a 1 ns rise time, the IW exits the tube at 34 ns, while for a 50 ns rise time the IW exits at 124 ns. Increasing the voltage rise time also produces a less intense IW. These two affects work together to reduce RONS production as the rise time increases.

The decrease in energy deposition with increasing voltage rise time significantly decreases energy deposition outside the tube, which affects production of excited states (O_2^*, O_2^{**}, and $N_2(v)$) to the greatest degree. Species which require reactions between multiple RONS are slightly more sensitive to voltage rise time than the average, with total fluences that decrease by 94%–97% as the rise time increases from 1 to 50 ns. The total fluences of the species that are least sensitive to rise time (O_3, O, N, H_2, NO, OH, and HO_2) still decrease by 80%–90% as the rise time increases. H_2 is the exception, as its production requires reaction between two H atoms, but it is one of the least sensitive species. As the energy deposition decreases, there is less O produced inside the tube, and less H is depleted in OH formation. This reduced competition for H at low energy deposition makes

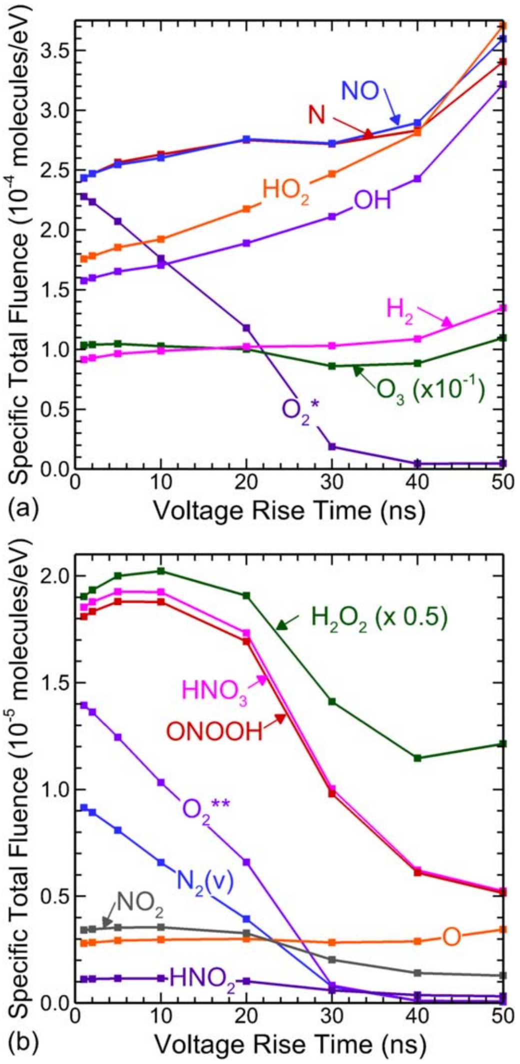

Figure 19. The total fluence of species collected at the pump per eV of energy deposition (specific total fluence) as a function of the voltage rise time. (a) O_2^*, O_3, OH, HO_2, H_2, N, and NO. (b) O_2^{**}, $N_2(v)$, O, H_2O_2, NO_2, HNO_2, HNO_3, and ONOOH.

H_2 less sensitive to the rise time than the other species which require reactions among RONS.

The specific total fluences for RONS are shown in figure 19 as function of voltage rise time. As the rise time increases and energy deposition decreases, the energy efficiency for species which require reactions among RONS (ONOOH, HNO_3, HNO_2, H_2O_2, and NO_2) generally decreases. At lower energy deposition (longer rise time), the dissociation fractions of impurities inside the tube are lower, and the RONS are less likely to interact with one another to form higher order species such as HNO_x, and instead survive until they reach the humid air and produce O_3 and HO_2. The specific total fluence of O_2^*, O_2^{**}, and $N_2(v)$ decrease most significantly with increasing rise time because these species are most sensitive to IW propagation outside of the tube.

3.9. Dielectric constant

The dielectric constant of the tube determines the local capacitance/unit-area ($F\,cm^{-2}$) which bounds the maximum surface charge on the inside of the tube for a given voltage. (The conductivity of the tube is negligible and so there no charge migration through the tube.) With a larger capacitance, a larger charge density is required to shield out the same applied voltage. The dielectric constant also affects the initial electric field profile. Higher dielectric constant materials expel the electric field in both the radial and axial directions. For the base case, increasing the dielectric constant reduces the electric field in the tube while increasing the electric field at the end of the tube. For example, for $\varepsilon_r = 20$, the IW is significantly weaker in the tube.

In the base case, $\varepsilon_r = 4$ and the energy deposition is 14.7 μJ. Above $\varepsilon_r = 4$, the energy deposition decreases with increasing ε_r (1.7 μJ for $\varepsilon_r = 20$) because the electric field inside the tube is weaker, and as a result the IW is less intense. This systematic reduction in energy deposition reduces the total fluence of all RONS exiting the computational domain with increasing ε_r, as shown in figure 20. For this electrode configuration energy deposition is maximum for $\varepsilon_r \approx 4$. At smaller ε_r, energy deposition is limited by the small capacitance of the tube at the powered electrode. For example, for $\varepsilon_r = 2$, energy deposition decreases to 12.1 μJ.

The specific total fluences as a function of ε_r are shown in figure 21. The energy efficiency of the production of species which do not require interaction among RONS, including O_3, O, N, NO, OH, and HO_2, generally increase with lower energy deposition and larger ε_r. H_2 also follows this trend because at higher energy deposition, H is more likely to react with O. The more complex RONS which require reaction among multiple RONS tend to have efficiencies that peak at higher energy deposition and lower ε_r. The excited states are produced preferentially in the cases of higher energy deposition (peaking at $\varepsilon_r = 4$) because these are also the conditions where the IW exits the tube the earliest. Again, higher energy deposition (ε_r closer to 4) favors the production of more complex RONS which requires reaction between several RONS. The excited states are also produced most efficiently near $\varepsilon_r \approx 4$, conditions for which the IW propagates the furthest outside of the tube.

The dielectric constant of the tube has a completely different effect on RONS production if the powered electrode is inside the tube, as shown by total fluences and specific total fluences in figures 22 and 23. For these results, the powered electrode inside the tube is separated from a ground ring electrode by 8 mm. As the dielectric constant increases, the IW propagates more slowly, because the capacitance of the tube is higher, and it takes more time to fully charge this capacitance. The IW exits the tube after 90 ns for $\varepsilon_r = 2$ compared to 170 ns for $\varepsilon_r = 12$. The total energy deposition increases from 185 μJ at $\varepsilon_r = 2$ to 493 μJ at $\varepsilon_r = 8$, and then decreases to 436 μJ at $\varepsilon_r = 12$. The energy deposited outside of the tube decreases from 6 μJ to 3 nJ as ε_r increases from 2 to 12, and n_e between the electrodes increases from 1×10^{14} to 7×10^{14} cm^{-3}.

Compared to the other parameters, the total fluences are relatively insensitive to the dielectric constant when the powered electrode is inside the tube, in spite of the energy deposition changing by nearly a factor of 3. Although energy

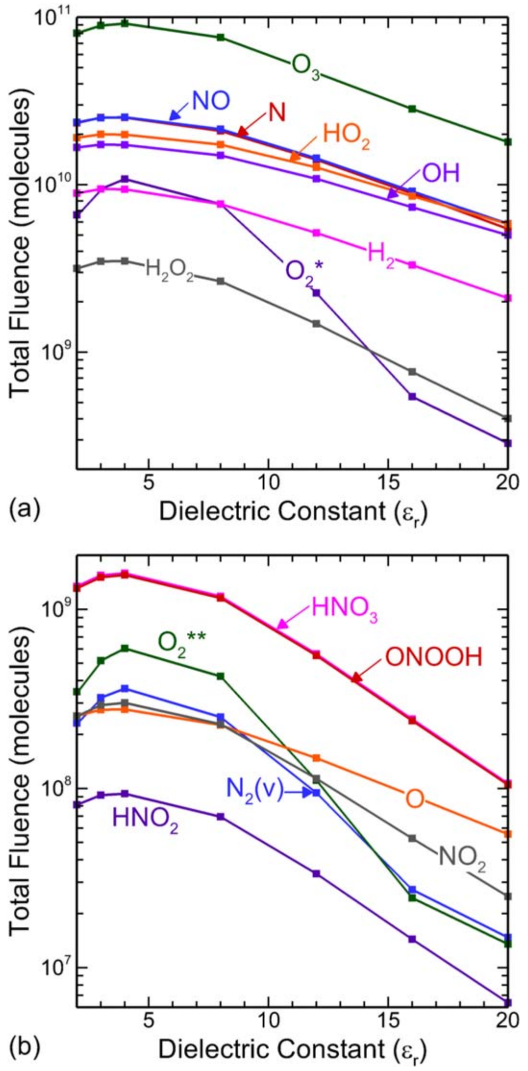

Figure 20. The total fluence of species exiting the computational domain as a function of dielectric constant for the configuration with the single powered electrode outside of the tube. The maximum production for all species occurs at $\varepsilon_r = 4$. (a) O_2^*, O_3, OH, H_2O_2, HO_2, H_2, N, and NO. (b) O_2^{**}, $N_2(v)$, O, NO_2, HNO_2, HNO_3, and ONOOH.

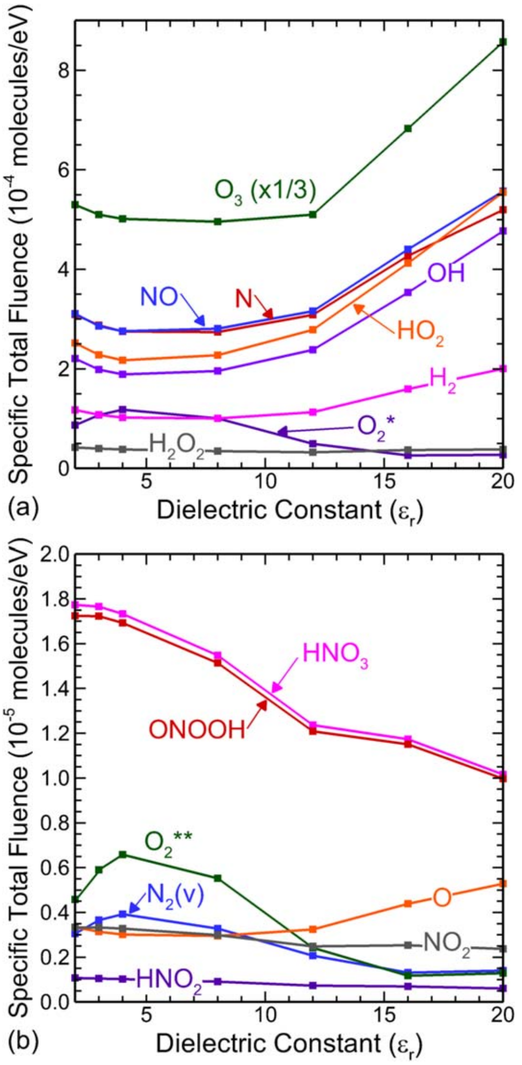

Figure 21. The total fluence of species collected at the pump per eV of energy deposition (specific total fluence) as a function of the dielectric constant of the tube for the configuration with a single powered electrode outside of the tube. (a) O_2^*, O_3, OH, H_2O_2, HO_2, H_2, N, and NO. (b) O_2^{**}, $N_2(v)$, O, NO_2, HNO_2, HNO_3, and ONOOH.

deposition is highest at $\varepsilon_r = 8$, the production of most species is largest at $\varepsilon_r = 4$ or $\varepsilon_r = 6$. These configurations have a larger energy deposition than $\varepsilon_r = 2$ with an IW that propagates further outside of the tube than $\varepsilon_r = 8$. The total fluences of excited states ($N_2(v)$, O_2^*, and O_2^{**}) are greatest at $\varepsilon_r = 3$ because they are more sensitive to propagation outside of the tube (which occurs at low ε_r) than the other species.

The specific total fluences of all species decrease as ε_r increases, with $N_2(v)$, O_2^*, and O_2^{**} decreasing the most, by more than 97%. The specific total fluences of most other species decrease by 60%–75% as the dielectric constant increases. The specific total fluences which are the least sensitive to ε_r are those for HO_2, H_2, and H_2O_2, which decrease by 55%–60%. Species which are formed by dissociation of H_2O are less sensitive to propagation of the IW outside of the tube. These species are more likely to be produced inside the tube, where they represent a larger fraction of the impurities.

4. Concluding remarks

Results from a computational investigation of helium APPJs flowing into humid air have demonstrated the importance of electrode configurations in the production of RONS. For an APPJ with a single powered ring electrode (and external electrical ground) the IW begins at the powered electrode, and upon exiting the tube follows the interface between the He and the surrounding humid air. Much of the RONS are produced at the interface between the He and humid air, but RONS are also produced in the tube due to impurities in the He flow. Moving ground planes closer to the plasma jet can increase the total energy deposition in the plasma for a

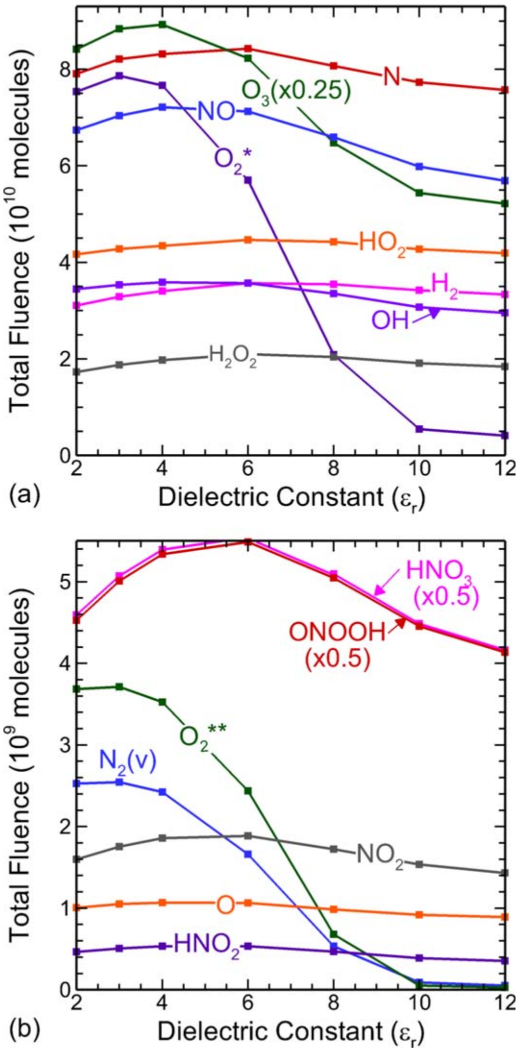

Figure 22. The total fluence of species exiting the computational domain as a function of the dielectric constant of the tube. The electrode configuration, shown in figure 15(a), has the powered electrode inside the tube and 8 mm between the electrodes. (a) O_2^*, O_3, OH, H_2O_2, HO_2, H_2, N, and NO. (b) O_2^{**}, N_2(v), O, NO_2, HNO_2, HNO_3, and ONOOH.

constant voltage, substantially influencing which RONS are produced and flow to surfaces, here referred as the total fluence. Total fluences of electronically excited states such as O_2^* are the most sensitive to these nearby ground planes, followed by species which require reactions among several RONS (e.g. HNO_2, HNO_3). Though the production of most RONS decrease as the ground plane is moved further from the jet, the specific total fluence (i.e., energy efficiency of production) of most species increases.

For configurations with a single powered ring electrode, moving the electrode closer to the outlet of the tube produces larger total fluences of all RONS as the total energy deposition increases. Depending on their origin, there is some selectivity of the total fluences of reactive species based on the placement of the ring electrode. For most species, the specific total fluence decreases as the electrode moves closer to the outlet.

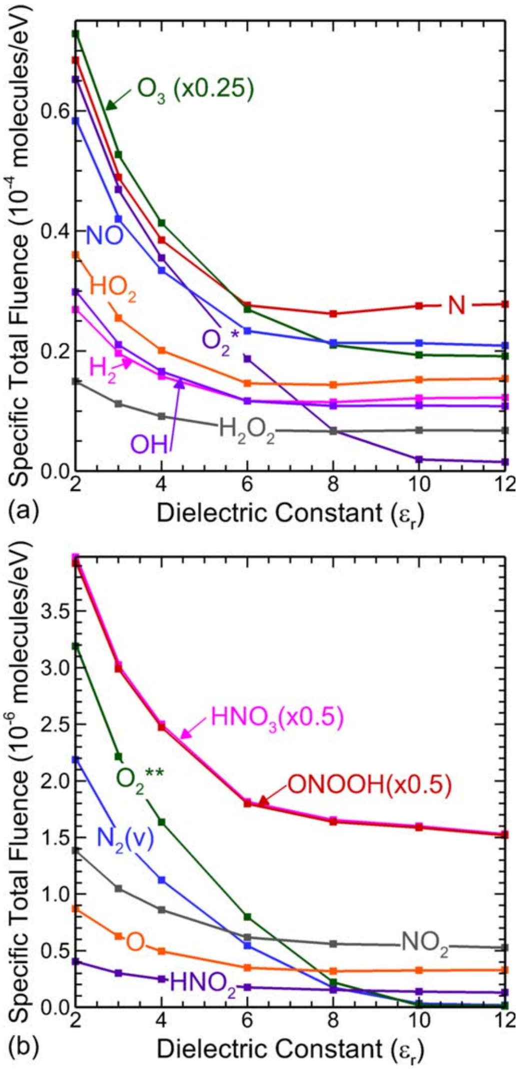

Figure 23. The total fluence of species collected at the pump per eV of energy deposition (specific total fluence) as a function of the dielectric constant of the tube. The electrode configuration, shown in figure 15(a), has the powered electrode inside the jet and 8 mm between the electrodes. (a) O_2^*, O_3, OH, H_2O_2, HO_2, H_2, N, and NO. (b) O_2^{**}, N_2(v), O, NO_2, HNO_2, HNO_3, and ONOOH.

Adding a grounded ring electrode to the APPJ results in more overall energy deposition for a constant voltage, most of which is deposited inside the tube between the electrodes. The IW propagates faster due to the higher electric field, but significantly slows when passing the grounded ring to charge the large capacitance of the dielectric tube at the ground electrode. Total fluences of species that require reactions among RONS, such as H_2, H_2O_2, HNO_3, ONOOH, NO_2, and HNO_2 are more sensitive to the addition of the grounded ring, and the total fluences of excited states such as O_2^* are most sensitive.

Moving the powered electrode inside the dielectric tube results in more rapid IW propagation, as the applied voltage is no longer shielded by the charging of the dielectric tube. The speed of the IW in this configuration is sensitive to the placement of the ground electrode, as are the total fluences of species that require reactions among several RONS.

Changing the position of the grounded electrode can significantly increase the energy deposition but decrease the total fluences of RONS as the volume of plasma between the electrodes is smaller. The RONS production then becomes limited by depletion of the molecular impurities in the He inside the tube. The energy efficiency of production of all RONS, with the exception of excited states such as O_2^*, decreases as energy deposition increases with the addition of a grounded ring.

For the two ring configuration (powered and grounded), increasing the gap between the electrodes tends to increase the total fluence of RONS. Though the electric fields are lower and the IW is less intense, the increased volume of the higher density plasma that forms between the electrodes increases the total fluences of RONS produced by the jet.

A shorter voltage rise time can significantly increase the total energy deposition in the plasma by producing a more intense IW. As a result, the total fluences of most species increase by about a factor of 10 as the rise time decreases from 50 ns to 1 ns. Short rise times increase the specific total fluences (energy efficiency) of RONS that require interaction between multiple plasma produced species, such as HNO_x. Longer rise times increase the specific total fluence of species that do not require reaction between RONS, such as NO and OH.

A dielectric constant of the tube material of $\varepsilon_r \approx 4$ produces maximum energy deposition into the plasma when the powered electrode is outside of the tube. Energy deposition for dielectric constants below this value is limited by the charging of the tube at the powered electrode. Dielectric constants in excess of $\varepsilon_r \approx 4$ expel the electric field from the tube, producing electric field enhancement only at the end of the tube, which produces a less intense IW in the tube. The efficiency of production of complex RONS is at a maximum when $\varepsilon_r \approx 4$ (higher energy deposition), while the efficiency is minimized for other RONS. If the electrode is inside the tube, increasing the dielectric constant results in slower IW propagation, and therefore an increase in energy deposition inside the tube, and a decrease in energy deposition outside of the tube.

Overall, the details of the configuration of the electrodes are important to both IW propagation dynamics and total fluences of RONS in He APPJs. Generally configurations which increase the energy deposited in the plasma increase the RONS production, but the efficiency of this production decreases. Small differences in design parameters between APPJs may produce significant disparities in RONS production. For example, it is important for the electrical grounds in the vicinity of APPJs to be controlled (and reported), as the proximity of these ground planes can have a substantial impact on IW propagation and the total fluences of RONS of a given APPJ. When comparing electrode configurations and reactive species production, it is important to consider not only the amount of energy coupled into the plasma, but also the location and volume over which this energy deposition occurs.

Acknowledgments

This work was supported by the Department of Energy Office of Fusion Energy Science (DE-SC000319, DE-SC0014132), the National Science Foundation (PHY-1519117) and the NSF Graduate Research Fellowship Program.

ORCID iDs

Amanda M Lietz https://orcid.org/0000-0001-6423-5042
Mark J Kushner https://orcid.org/0000-0001-7437-8573

References

[1] Dobrynin D *et al* 2011 *Plasma Med.* **1** 93
[2] Arndt S *et al* 2013 *PLoS One* **8** e79325
[3] Brehmer F, Haenssle H A, Daeschlein G, Ahmed R, Pfeiffer S, Görlitz A, Simon D, Schön M P, Wandke D and Emmert S 2014 *J. Eur. Acad. Dermatol. Venereol.* **29** 148
[4] Joh H M, Kim S J, Chung T H and Leem S H 2012 *Appl. Phys. Lett.* **101** 053703
[5] Vandamme M, Robert E, Dozias S, Sobilo J, Lerondel S, Le Pape A and Pouvesle J-M 2011 *Plasma Med.* **1** 27
[6] Mizuno K, Yonetamari K, Shirakawa Y, Akiyama T and Ono R 2017 *J. Phys. D: Appl. Phys.* **50** 12LT01
[7] Graves D B 2012 *J. Phys. D: Appl. Phys.* **45** 263001
[8] Graves D B 2014 *Clin. Plasma Med.* **2** 38
[9] Kaushik N, Uddin N, Sim G B, Hong Y J, Baik K Y, Kim C H, Lee S J, Kaushik N K and Choi E H 2015 *Nat. Sci. Rep.* **5** 8587
[10] Bauer G and Graves D B 2016 *Plasma Process. Polym.* **13** 1157
[11] Ke Z, Thopan P, Fridman G, Miller V, Yu L, Fridman A and Huang Q 2017 *Clin. Plasma Med.* **7–8** 1
[12] Winter J, Brandenburg R and Weltmann K-D 2015 *Plasma Sources Sci. Technol.* **24** 064001
[13] Xu H, Chen C, Liu D, Xu D and Liu Z 2017 *J. Phys. D: Appl. Phys.* **50** 245201
[14] Winter J *et al* 2014 *J. Phys. D: Appl. Phys.* **47** 285401
[15] Bartis E A J, Luan P, Knoll A J, Hart C, Seog J and Oehrlein G S 2015 *Biointerphases* **10** 029512
[16] Maletić D, Puač N, Malović G, Đorđević A and Petrović Z L 2017 *J. Phys. D: Appl. Phys.* **50** 145202
[17] Jõgi I, Talviste R, Raud J, Piip K and Paris P 2014 *J. Phys. D: Appl. Phys.* **47** 415202
[18] Maletić D, Puač N, Selaković N, Lazović S, Malović G, Đorđević A and Petrović Z L 2015 *Plasma Sources Sci. Technol.* **24** 025006
[19] Yue Y, Pei X and Lu X 2016 *J. Appl. Phys.* **119** 033301
[20] Norberg S A, Johnsen E and Kushner M J 2015 *Plasma Sources Sci. Technol.* **24** 035026
[21] Van Gaens W and Bogaerts A 2014 *J. Phys. D: Appl. Phys.* **47** 079502
[22] Kelly S and Turner M M 2014 *Plasma Sources Sci. Technol.* **23** 065013
[23] Pitchford L C and Phelps A V 1982 *Phys. Rev.* A **25** 540
[24] Gallagher J W, Brion C E, Samson J A R and Langhoff P W 1988 *J. Phys. Chem. Ref. Data* **17** 9
[25] Scharfetter D L and Gummel H K 1969 *IEEE Trans. Electron Devices* **16** 64
[26] Norberg S 2015 Modeling atmospheric pressure plasma jets: plasma dynamics, interaction with dielectric surfaces, liquid layers and cells *PhD Thesis* University of Michigan http://hdl.handle.net/2027.42/113342

[27] Schröter S, Gibson A R, Kushner M J, Gans T and O'Connell D 2018 *Plasma Phys. Control. Fusion* **60** 014035

[28] Lu X, Laroussi M and Puech V 2012 *Plasma Sources Sci. Technol.* **21** 034005

[29] Darny T, Pouvesle J-M, Puech V, Douat C, Dozias S and Robert E 2017 *Plasma Sources Sci. Technol.* **26** 045008

[30] Liu D X, Bruggeman P, Iza F, Rong M Z and Kong M G 2010 *Plasma Sources Sci. Technol.* **19** 025018

[31] van Ham B T J, Hofmann S, Brandenburg R and Bruggeman P J 2014 *J. Phys. D: Appl. Phys.* **47** 224013

[32] Verreycken T, Mensink R, van der Horst R, Sadeghi N and Bruggeman P J 2013 *Plasma Sources Sci. Technol.* **22** 055014

[33] Klarenaar B L M, Guaitella O, Engeln R and Sobota A 2018 *Plasma Sources Sci. Technol.* **27** 085004

[34] Kovačević V V, Sretenović G B, Slikboer E, Guaitella O, Sobota A and Kuraica M M 2018 *J. Phys. D: Appl. Phys.* **51** 065202

[35] Yonemori S and Ono R 2014 *J. Phys. D: Appl. Phys.* **47** 125401